

GEORGIA DOT RESEARCH PROJECT 19-16

Final Report

**IMPROVEMENT OF CLIMATE DATA FOR
USE IN MEPDG CALIBRATION AND OTHER
PAVEMENT ANALYSIS – PHASE II**



Georgia Department of Transportation

**Office of Performance-based
Management and Research**

600 West Peachtree Street NW
Atlanta, GA 30308

1. Report No.: FHWA-GA-21-1916	2. Government Accession No.: N/A	3. Recipient's Catalog No.: N/A	
4. Title and Subtitle: Improvement of Climate Data for Use in MEPDG Calibration and Other Pavement Analysis – Phase II		5. Report Date: February 2021	
		6. Performing Organization Code: N/A	
7. Author(s): Stephan A. Durham, Ph.D., P.E. (https://orcid.org/0000-0002-6177-3491); Bora Cetin, Ph.D.; Charles W. Schwartz, Ph.D.; Barton A. Forman, Ph.D.; and Shafkat Alam-Khan		8. Performing Organization Report No.: 19-16	
9. Performing Organization Name and Address: University of Georgia College of Engineering Driftmier Engineering Center, Athens, GA. 30602 Phone: (706) 542-9480 Email: sdurham@uga.edu		10. Work Unit No.: N/A	
		11. Contract or Grant No.: PI# 0016503	
12. Sponsoring Agency Name and Address: Georgia Department of Transportation Office of Performance-based Management and Research 600 West Peachtree St. NW Atlanta, GA 30308		13. Type of Report and Period Covered: Final; August 2019 – February 2021	
		14. Sponsoring Agency Code: N/A	
15. Supplementary Notes: Prepared in cooperation with the U.S. Department of Transportation, Federal Highway Administration.			
16. Abstract: Pavement temperature is one of the most important parameters that influence pavement performance. In the Pavement ME Design (PMED) software, the pavement temperatures are determined based on the shortwave radiation (SWR) and longwave radiation (LWR) models. In this project, the accuracy of such radiation models is assessed. The PMED-recommended net SWR and the downwelling and upwelling LWR models were found in this study to be physically inconsistent and inaccurate. Alternative SWR data sources were identified in the Modern Era Retrospective Analysis for Research and Application, version 2 (MERRA-2) database. In addition, the research team identified alternative LWR models through an extensive literature review. Such SWR and LWR models provide superior estimations and, therefore, eliminate nearly all the issues associated with the PMED-recommended radiation models. Finally, asphalt concrete (AC) pavement distresses were analyzed for seven different radiation models via software called Mechanistic–Empirical Asphalt Pavement Analysis (MEAPA) software. It was determined that modifications in the radiation models significantly impact the pavement distresses. Based on such results, this study recommends that the net SWR, as well as the downwelling and upwelling LWR models, be updated in PMED, as outlined in this report.			
17. Keywords: Flexible pavement analysis; climate effects; solar radiation models; Mechanistic–Empirical Pavement Design Guide (MEPDG); Pavement ME Design (PMED); Mechanistic–Empirical Asphalt Pavement Analysis (MEAPA); Modern Era Retrospective Analysis for Research and Applications (MERRA)			18. Distribution Statement: No Restriction
19. Security Classification (of this report): Unclassified	20. Security Classification (of this page): Unclassified	21. No. of Pages: 76	22. Price: Free

GDOT Research Project 19-16

Final Report

**IMPROVEMENT OF CLIMATE DATA FOR USE IN MEPDG CALIBRATION
AND OTHER PAVEMENT ANALYSIS – PHASE II**

By

Stephan A. Durham, Ph.D., P.E.

Professor – College of Engineering

Bora Cetin, Ph.D.

Associate Professor – Department of Civil and Environmental Engineering

Charles W. Schwartz, Ph.D.

Professor – Department of Civil and Environmental Engineering

Barton A. Forman, Ph.D.

The Deborah J. Goodings Associate Professor – Department of Civil and Environmental
Engineering

Shafkat Alam-Khan

Graduate Research Assistant

University of Georgia

Michigan State University

University of Maryland

Contract with

Georgia Department of Transportation

In cooperation with

U.S. Department of Transportation

Federal Highway Administration

February 2021

The contents of this report reflect the views of the authors, who are responsible for the facts and accuracy of the data presented herein. The contents do not necessarily reflect the official views of the Georgia Department of Transportation or the Federal Highway Administration. This report does not constitute a standard, specification, or regulation.

SI* (MODERN METRIC) CONVERSION FACTORS

APPROXIMATE CONVERSIONS TO SI UNITS

Symbol	When You Know	Multiply By	To Find	Symbol
LENGTH				
in	inches	25.4	millimeters	mm
ft	feet	0.305	meters	m
yd	yards	0.914	meters	m
mi	miles	1.61	kilometers	km
AREA				
in ²	square inches	645.2	square millimeters	mm ²
ft ²	square feet	0.093	square meters	m ²
yd ²	square yard	0.836	square meters	m ²
ac	acres	0.405	hectares	ha
mi ²	square miles	2.59	square kilometers	km ²
VOLUME				
fl oz	fluid ounces	29.57	milliliters	mL
gal	gallons	3.785	liters	L
ft ³	cubic feet	0.028	cubic meters	m ³
yd ³	cubic yards	0.765	cubic meters	m ³
NOTE: volumes greater than 1000 L shall be shown in m ³				
MASS				
oz	ounces	28.35	grams	g
lb	pounds	0.454	kilograms	kg
T	short tons (2000 lb)	0.907	megagrams (or "metric ton")	Mg (or "t")
TEMPERATURE (exact degrees)				
°F	Fahrenheit	5 (F-32)/9 or (F-32)/1.8	Celsius	°C
ILLUMINATION				
fc	foot-candles	10.76	lux	lx
fl	foot-Lamberts	3.426	candela/m ²	cd/m ²
FORCE and PRESSURE or STRESS				
lbf	poundforce	4.45	newtons	N
lbf/in ²	poundforce per square inch	6.89	kilopascals	kPa

APPROXIMATE CONVERSIONS FROM SI UNITS

Symbol	When You Know	Multiply By	To Find	Symbol
LENGTH				
mm	millimeters	0.039	inches	in
m	meters	3.28	feet	ft
m	meters	1.09	yards	yd
km	kilometers	0.621	miles	mi
AREA				
mm ²	square millimeters	0.0016	square inches	in ²
m ²	square meters	10.764	square feet	ft ²
m ²	square meters	1.195	square yards	yd ²
ha	hectares	2.47	acres	ac
km ²	square kilometers	0.386	square miles	mi ²
VOLUME				
mL	milliliters	0.034	fluid ounces	fl oz
L	liters	0.264	gallons	gal
m ³	cubic meters	35.314	cubic feet	ft ³
m ³	cubic meters	1.307	cubic yards	yd ³
MASS				
g	grams	0.035	ounces	oz
kg	kilograms	2.202	pounds	lb
Mg (or "t")	megagrams (or "metric ton")	1.103	short tons (2000 lb)	T
TEMPERATURE (exact degrees)				
°C	Celsius	1.8C+32	Fahrenheit	°F
ILLUMINATION				
lx	lux	0.0929	foot-candles	fc
cd/m ²	candela/m ²	0.2919	foot-Lamberts	fl
FORCE and PRESSURE or STRESS				
N	newtons	0.225	poundforce	lbf
kPa	kilopascals	0.145	poundforce per square inch	lbf/in ²

* SI is the symbol for the International System of Units. Appropriate rounding should be made to comply with Section 4 of ASTM E380. (Revised March 2003)

TABLE OF CONTENTS

CHAPTER 1. INTRODUCTION	1
Overview	1
Problem Statement	3
Research Objectives	4
Significance of the Research	4
Organization of the Report	5
CHAPTER 2. BACKGROUND AND LITERATURE REVIEW	6
Climate Data Sources for PMED Analyses	6
Earth Energy Balance System	8
Radiation Models Used in PMED Analyses	9
CHAPTER 3. RESEARCH METHODOLOGY	14
Evaluation of Shortwave and Longwave Radiation Models	14
Shortwave and Longwave Radiation Models Used in Pavement Distress Analyses	15
Mechanistic–Empirical Asphalt Pavement Analysis	17
Design Inputs Used to Analyze Pavement Distresses	18
CHAPTER 4. RESULTS	20
Evaluation of Downwelling Shortwave Radiation Model	20
Evaluation of Downwelling Longwave Radiation Model	21
Impacts of the Shortwave and Longwave Radiation Models in Pavement Distresses and Temperature Profiles Predictions	26
Total Rutting Predictions	26
Asphalt Layer Rutting Predictions.....	31
Bottom-up Fatigue Cracking Predictions	36
Pavement Surface Temperature Predictions	41
CHAPTER 5. CONCLUSIONS AND RECOMMENDATIONS	47
Summary and Conclusions	47
Recommendations	50

APPENDIX A: Extraction of MERRA-2 Data.....	52
APPENDIX B: Implementation and Integration of SWR and LWR Models in PMED	58
ACKNOWLEDGMENTS	62
REFERENCES	63

LIST OF FIGURES

Figure 1. Image. Earth’s energy balance system. (NASA 2014).....	9
Figure 2. Image. Locations of the SIRS stations (black dots) used in the analysis.	15
Figure 3. Image. Locations of the test locations (green circles) used in the regional analysis.	18
Figure 4. Graph. Probability plots of calculated D-SWR values based on MERRA-2 against the SIRS observations of D-SWR.	21
Figure 5. Graphs. Probability plots of observed and modeled radiation fluxes for (a) D-LWR flux assuming clear-sky conditions, and (b) D-LWR flux during all-sky conditions including cloud amplification.	22
Figure 6. Graphs. Probability plots of observed and modeled radiation fluxes for (a) D-LWR flux assuming clear-sky conditions; and (b) D-LWR flux during all-sky conditions, including cloud amplification.	23
Figure 7. Graphs. Probability plots of observed and modeled radiation fluxes for (a) D-LWR flux assuming clear-sky conditions; and (b) D-LWR flux during all-sky conditions, including cloud amplification.	24
Figure 8. Graphs. Probability plots of observed and modeled radiation fluxes for (a) D-LWR flux assuming clear-sky conditions; and (b) D-LWR flux during all-sky conditions, including cloud amplification effects.....	25
Figure 9. Graph. Impacts of radiation models on total rutting prediction in Clayton, GA.....	27
Figure 10. Graph. Impacts of radiation models on total rutting prediction in Donalsonville, GA.	28
Figure 11. Graph. Impacts of radiation models on total rutting prediction in Jeffersonville, GA.....	29
Figure 12. Graph. Impacts of radiation models on total rutting prediction in Trenton, GA.	30
Figure 13. Graph. Impacts of radiation models on total rutting prediction in Woodbine, GA.	31
Figure 14. Graph. Impacts of radiation models on asphalt layer rutting prediction in Clayton, GA.....	32
Figure 15. Graph. Impacts of radiation models on asphalt layer rutting prediction in Donalsonville, GA.	33
Figure 16. Graph. Impacts of radiation models on asphalt layer rutting prediction in Jeffersonville, GA.....	34

Figure 17. Graph. Impacts of radiation models in asphalt layer rutting prediction in Trenton, GA.....	35
Figure 18. Graph. Impacts of radiation models on asphalt layer rutting prediction in Woodbine, GA.....	36
Figure 19. Graph. Impacts of radiation models on bottom-up fatigue cracking prediction in Clayton, GA.....	37
Figure 20. Graph. Impacts of radiation models on bottom-up fatigue cracking prediction in Donalsonville, GA.....	38
Figure 21. Graph. Impacts of radiation models on bottom-up fatigue cracking prediction in Jeffersonville, GA.....	39
Figure 22. Graph. Impacts of radiation models on bottom-up fatigue cracking prediction in Trenton, GA.....	40
Figure 23. Graph. Impacts of radiation models on bottom-up fatigue cracking prediction in Woodbine, GA.....	41
Figure 24. Graph. Impacts of radiation models on pavement surface temperature in Clayton, GA.....	42
Figure 25. Graph. Impacts of Radiation Models on Pavement Surface Temperature in Donalsonville, GA.....	43
Figure 26. Graph. Impacts of radiation models on pavement surface temperature prediction in Jeffersonville, GA.....	44
Figure 27. Graph. Impacts of radiation models on pavement surface temperature prediction in Trenton, GA.....	45
Figure 28. Graph. Impacts of radiation models on pavement surface temperature prediction in Woodbine, GA.....	46
Figure 29. Image. LTPP climate tool page.....	54
Figure 30. Image. Data attributes selection.....	55
Figure 31. Image. Add to data bucket.....	56
Figure 32. Image. Go to data bucket.....	56
Figure 33. Image. Submit for data extraction.....	57

LIST OF TABLES

Table 1. Summary of the MERRA-2 stations used in the analyses.....	19
Table 2. Traffic and AC pavement layer thicknesses.	19
Table 3. AC pavement design properties.....	19
Table 4. AC surface layer properties.	19

EXECUTIVE SUMMARY

In the Pavement ME Design (PMED) software, environmental impacts on pavement responses are modeled via a sophisticated climate modeling tool: the Enhanced Integrated Climate Model (EICM). The EICM is a one-dimensional coupled heat and moisture flow program. It simulates the temperature and moisture profiles for each pavement layer over the design life.

Pavement surface temperature is one of the most important parameters in predicting the performance of flexible pavements. The pavement surface temperature depends on the earth's heat balance system. The solar energy enters into the earth system as downwelling shortwave radiation (D-SWR). The ground emits energy as upwelling longwave radiation (U-LWR). A portion of the U-LWR reflects from the cloud and returns to the earth as downwelling longwave radiation (D-LWR). Thus, the pavement surface temperature is a function of the D-SWR, D-LWR, and U-LWR.

PMED estimates the D-SWR, D-LWR, and U-LWR based on empirical models. Such empirical models are based on nonfundamental properties, such as cloud cover. In this study, the accuracy of the PMED-recommended, as well as multiple alternative SWR and LWR models, were assessed. The ground-based radiation observation data, which were collected from 21 solar infrared radiation stations (SIRS) located in the Southern Great Plains of the United States (U.S.), were used as ground truth. It was evidenced that the PMED-recommended (Dempsey et al. 1985) D-SWR, D-LWR, and U-LWR models were physically inconsistent. D-SWR estimates from Modern Era Retrospective Analysis for Research and Applications, version 2 (MERRA-2) and D-LWR estimates from the Idso (1981) model were physically consistent, as evidenced in this study. In addition, it was

determined that a more physically consistent U-LWR parameterization does not include a cloud correction factor as proposed by Dempsey et al. (1985) and, therefore, the PMED-recommended U-LWR model was modified accordingly. Seven analysis cases were defined for different SWR and LWR models, which are summarized as follows:

- **Case 1:** Unmodified PMED model
- **Case 2:** Updated D-SWR model
- **Case 3:** Updated D-SWR and D-LWR model (with constant vapor pressure data)
- **Case 4:** Updated D-SWR and U-LWR model (with constant vapor pressure data)
- **Case 5:** Updated D-SWR, D-LWR and U-LWR model (with constant vapor pressure)
- **Case 6:** Updated D-SWR and D-LWR model (with hourly variable vapor pressure)
- **Case 7:** Updated D-SWR, D-LWR and U-LWR model (with hourly variable vapor pressure)

Pavement distresses predicted via cases 1 (unmodified PMED method), 2 (updated D-SWR), 5 (updated LWR with constant vapor pressure), and 7 (updated LWR with dynamic vapor pressure) were highlighted in this study. Among these, analysis case 7 represents the most accurate radiation models. Analysis cases 3, 4, and 6 illustrated hypothetical conditions with limited practical significance. Such hypothetical cases were defined to observe the unit response of pavement distresses for changing each radiation model.

A mechanistic–empirical flexible pavement design and analysis software, called Mechanistic–Empirical Asphalt Pavement Analysis (MEAPA), was utilized to assess the

impacts of these analysis cases on pavement responses. Climate data for the MEAPA simulation were collected from five cities located in Georgia. The predicted pavement distresses were significantly influenced as a result of using the updated SWR and LWR models, as evidenced in this study. All analyses use global field calibration factors similar to PMED. For case 1 (unmodified PMED), the average total rutting, average asphalt layer rutting, average bottom-up fatigue cracking, and average pavement surface temperature estimates were 0.23 inch, 0.07 inch, 0.02 percent, and 18.5°C, respectively. When the shortwave radiation model was updated (case 2), the average total rutting, average asphalt layer rutting, average bottom-up fatigue cracking, and average pavement surface temperature estimates increased to 0.30 inch, 0.14 inch, 0.06 percent, and 23.6°C, respectively. After the D-LWR model was modified (case 3), the average total rutting, average asphalt layer rutting, average bottom-up fatigue cracking, and average pavement surface temperature estimates increased to 0.45 inch, 0.28 inch, 0.28 percent, and 33.5°C, respectively. As a result of changing the U-LWR model (case 4), the average total rutting, average asphalt layer rutting, average bottom-up fatigue cracking, and average pavement surface temperature estimates decreased to 0.18 inch, 0.03 inch, 0.00 percent, and 3.3°C, respectively. When both the U-LWR and D-LWR models were updated with constant-value vapor pressure data (case 5), the average total rutting, average asphalt layer rutting, average bottom-up fatigue cracking, and average pavement surface temperature estimates increased to 0.36 inch, 0.20 inch, 0.14 percent, and 29.4°C. After the D-LWR model was updated with dynamic vapor pressure data (case 6), the average total rutting, average asphalt layer rutting, average bottom-up fatigue cracking, and average pavement surface temperature estimates increased to 0.48 inch, 0.31 inch, 0.30 percent, and 33.0°C,

respectively. Finally, as a result of using the U-LWR and D-LWR models with dynamic vapor pressure data (case 7), the average total rutting, average asphalt layer rutting, average bottom-up fatigue cracking, and average pavement surface temperature estimates were 0.38 inch, 0.21 inch, 0.15 percent, and 28.8°C, respectively. Based on these results, the conclusions are summarized as follows:

- PMED-recommended SWR and LWR models are sometimes physically inconsistent and inaccurate.
- MERRA-2 provides physically consistent D-SWR estimates.
- D-LWR estimates based on Idso (1981) are physically consistent.
- The U-LWR model proposed by Dempsey et al. (1985) includes a redundant cloud correction factor.
- Pavement distress predictions were significantly impacted as a result of updating the radiation models.
- Updates in SWR models had more of an effect on pavement distress and temperature profiles, compared to updates in LWR models.
- Pavement distress and temperature predictions were mildly influenced when time-varying vapor pressure data were utilized to analyze atmospheric emissivity instead of using a constant-value vapor pressure of 10 mm Hg, as recommended by PMED.

Based on these conclusions, the research team recommends updating the D-SWR, D-LWR, and U-LWR models in the PMED background algorithms, as described in the report.

CHAPTER 1. INTRODUCTION

OVERVIEW

The American Association of State Highway and Transportation Officials' (AASHTO's) empirical pavement design was developed based on road tests conducted during the 1950s in Illinois (AASHTO 1993). During those road tests; one type of subgrade and base materials were considered. The construction quality was above average for those test sections. In addition, the present-day traffic types and volumes significantly differ from those of 1950. Such limitations of the empirical pavement design method were addressed during the development of the *Mechanistic–Empirical Pavement Design Guide* (MEPDG) and the Pavement ME Design (PMED) software. In the early 2000s, the MEPDG was developed through the efforts of the National Cooperative Highway Research Program (NCHRP 2004). The PMED software was developed based on the MEPDG documentations (AASHTO 2015). In PMED analyses, the traffic, climate, and material properties, as well as the pavement structural properties and design features are analyzed to estimate the primary pavement responses, such as stress, strain, and deflection. Such primary responses are further analyzed to predict the pavement performance. Pavement distresses such as rutting, fatigue cracking, and thermal cracking are determined through material-level phenomenological models and transfer functions. Local calibration can improve the accuracy of the transfer functions to predict such pavement distresses. Adoption of mechanistic–empirical pavement design offers a couple of benefits since it can incorporate the effects of a broader range of vehicle types, material properties, and climatic effects. The PMED method can characterize the existing pavement surface for

rehabilitation purposes. The advantages of the mechanistic–empirical methods are as follows:

- The effects of the tire loads, axle and tire configurations, repetition of loads, distribution of traffic, and wheel wander are considered in the analysis.
- The engineering properties of portland cement concrete (PCC), asphalt concrete (AC), base, subbase, and subgrade layers are considered for material characterization.
- The climatic impacts are characterized in the Enhanced Integrated Climate Module (EICM) to predict the effects of temperature, relative humidity, sunshine, wind speed, and precipitation on the pavement performance.
- The design features, such as widened slab, joint spacing, and doweled bar specifications, are considered in the analysis process.
- Characterization of existing pavement layers and new materials are considered.
- The results provide improved reliability prediction for the pavement infrastructure.

The Enhanced Integrated Climate Module is a sophisticated climatic modeling tool that was incorporated in PMED. The EICM is a one-dimensional coupled heat and moisture program. It simulates the temperature and moisture profiles of the pavement layers, sublayers, and subgrade over the lifetime. Such seasonal fluctuations of the temperature and moisture influence the material characteristics. The EICM models the impacts of the moisture on the base, subbase, and subgrade layers and the effects of temperature for all the bound and unbound pavement layers. As a result of the environmental effects, pavement deterioration processes such as thermal cracking, frost heaving, thawing, and

utting are influenced. Therefore, accurate and reliable climatic data inputs are essential for realistic pavement performance predictions. The EICM requires at least 2 years of hourly cloud cover, precipitation, wind speed, air temperature, and relative humidity data for computational purposes. However, a significant amount of reliable and accurate data can assist the program in conducting a robust and detailed analysis. Even one-decade-long climate data can be susceptible to outliers and, therefore, the EICM accuracies and pavement performance predictions will be impacted.

PROBLEM STATEMENT

Over the decades, significant research efforts have been made to obtain high-quality climatic data for PMED analyses (Brink et al. 2017; Cetin et al. 2018; Durham et al. 2019; Gelaro et al. 2017; Johanneck and Khazanovich 2010; Kalnay et al. 1996; Onogi et al. 2005; Rienecker et al. 2011; Schwartz 2015; Schwartz et al. 2015; Uppala et al. 2005; Zaghoul et al. 2006). However, limited research was conducted to assess the accuracy of the climatic algorithms (the EICM) of PMED. Pavement surface temperature is one of the most important parameters that influence the pavement performance (Faisal et al. 2016; Islam et al. 2014; Khan et al. 2017a; Khan et al. 2017b; Khan et al. 2019). Pavement surface temperature depends on the earth's heat energy balance from solar and heat radiations. PMED utilizes empirical models to estimate the radiation parameters. Such models are dependent on nonfundamental properties, such as cloud cover. Cloud cover is a poorly defined parameter since the cloud types, altitude, and thickness are not considered. Inaccurate radiation models can significantly undermine the credibility of the PMED analyses since clouds have significant impacts on downwelling shortwave radiation (D-SWR) and downwelling longwave radiation (D-LWR) (Sugita and Brutsaert 1993;

Várnai and Davies 1999). In the pavement engineering community, limited research was conducted to assess the accuracy of radiation models that are recommended by PMED.

RESEARCH OBJECTIVES

The goals of this project were to assess the accuracy of the radiation models that are recommended by PMED and investigate the impacts of radiation models in pavement distress analyses. To accomplish these goals, the research team successfully completed the following objectives.

- Additional validation of Modern Era Retrospective Analysis for Research and Applications, version 2 (MERRA-2) shortwave radiation (SWR) predictions.
- Critical review of EICM longwave radiation (LWR) modeling.
- Development of improved LWR modeling for EICM.
- Validation of improved LWR modeling.
- Assessment of improved LWR modeling on pavement performance predictions.

SIGNIFICANCE OF THE RESEARCH

The primary benefit of this study is a more comprehensive evaluation of the effects of LWR on pavement performance and establishment of a framework on how MERRA-2 should be implemented to provide both SWR and LWR inputs into PMED. Ultimately, this study provides appropriate supporting information and recommendations that can be implemented by the Georgia Department of Transportation (GDOT) and presented to the AASHTO Pavement ME Task Force committee for future consideration and adoption. The outcomes of this study can aid in the future improvement of pavement performance prediction by providing more accurate climate inputs for PMED.

ORGANIZATION OF THE REPORT

Chapter 1 introduces the problem statement and research significance of the project. Chapter 2 includes the background and literature review on the radiation models that are utilized for PMED analyses. A description of is research methodology used in the study is presented in chapter 3. Chapter 4 shows the analyses and results of the study. Conclusions and recommendations are included in chapter 5.

CHAPTER 2. BACKGROUND AND LITERATURE REVIEW

CLIMATE DATA SOURCES FOR PMED ANALYSES

Environmental conditions significantly impact pavement performance and its service life. Therefore, it is important to take the effects of environmental conditions into account during pavement design analyses. Collecting data for each input has been a major challenge for agencies. Climate input affects the overall pavement performance, as critical material properties change with fluctuating moisture and temperature conditions (Andrey et al. 2013). Johanneck and Khazanovich (2010) compared the PMED pavement performance predictions for composite pavements consisting of asphalt cement over portland cement concrete for 610 locations across the United States. Their study assessed the quality of climate data available in PMED and concluded that the database was non-uniform and of low quality. One of the conclusions of the study was that these data were not reliable in mountainous regions. Breakah et al. (2011) also investigated the effects of the accuracy of climatic data on pavement performance through PMED. Their study analyzed and compared the climatic files available within PMED and the ones developed based on the historical information for counties in the state of Iowa through a source called the Iowa Environmental Mesonet (IEM). Data from 24 counties across Iowa were used to represent the climate data for 99 counties in Iowa. Analyses were conducted for each county using both the PMED default climatic files and the IEM climatic files. Results showed that distresses predicted via these two sources (i.e., PMED and IEM files) were similar. However, IEM files provided more uniform climatic data sources compared to those embedded in PMED.

Cetin et al. (2018) and Schwartz et al. (2015) integrated the hourly MERRA, version 1 (MERRA-1) estimates into the PMED software. As part of their work, statistical analyses for the PMED weather input data from ground-based weather stations and the nearest MERRA-1 grid cell were conducted. Their studies showed that the differences in weather statistics between the MERRA-1 and ground-based weather station data were generally small for hourly temperatures.

PMED analyses in the two studies were conducted in order to compare the pavement distresses predicted via: (1) weather data embedded with the PMED software, (2) weather data collected from ground-based weather stations (GBWSs) throughout South Dakota and neighboring states, and (3) MERRA-1 meteorological estimates. Overall, the comparisons of the pavement distresses for both flexible and rigid pavements predicted using MERRA-1 vs. PMED weather data, MERRA-1 vs. GBWS data, and PMED weather data vs. GBWS data are all similar in value. The overall conclusion from Cetin et al. (2018) and Schwartz et al. (2015) was that MERRA-1 data provides better accuracy and spatial continuity than the data from ground-based weather stations, including the weather data accompanying the MEPDG software. In addition, MERRA-1 data were continuous in space and time and undergo significant quality checks.

Phase I of GDOT Research Project 16-10 studied the use of SWR to back-calculate the synthetic percent sunshine in the climatic files collected from MERRA-2 and MERRA-1 (Durham et al. 2019). Comparisons of predicted pavement performance using MERRA-1 vs. MERRA-2 climate data and their respective synthetic percent sunshine histories showed dramatically improved agreement for both flexible and rigid pavements, with the predictions clustered tightly along their respective lines of equality. Phase I of the

study recommended re-evaluation of the percent sunshine approach currently used in PMED. Percent sunshine as obtained from percent cloud cover, whether measured or predicted, is a nonfundamental derived property that is too imprecise for use in pavement performance modeling. It was recommended to convert SWR as the direct input to PMED for pavement environmental modeling.

Percent sunshine is also used in the PMED environmental modeling for adjusting the net LWR impinging on the pavement. The importance of this LWR and its adjustment for cloud cover has not been investigated for pavement performance prediction analyses in the literature.

EARTH ENERGY BALANCE SYSTEM

The components of solar (i.e., SWR) and heat (i.e., LWR) radiation are illustrated in figure 1. These components are the primary environmental input influencing pavement temperatures. Approximately 50 percent (on an annual average basis) of the downwelling shortwave radiation (yellow arrows in figure 1) at the top of the atmosphere is reflected by clouds or absorbed by the atmosphere. Approximately 80 to 90 percent of the SWR reaching the surface is ultimately absorbed by the pavement, causing pavement heating. The heated pavement in turn emits upwelling longwave radiation (U-LWR) (red arrows in figure 1). A substantial portion of this is returned as downwelling longwave radiation to the surface by the emissions and reflections from clouds and the atmosphere.

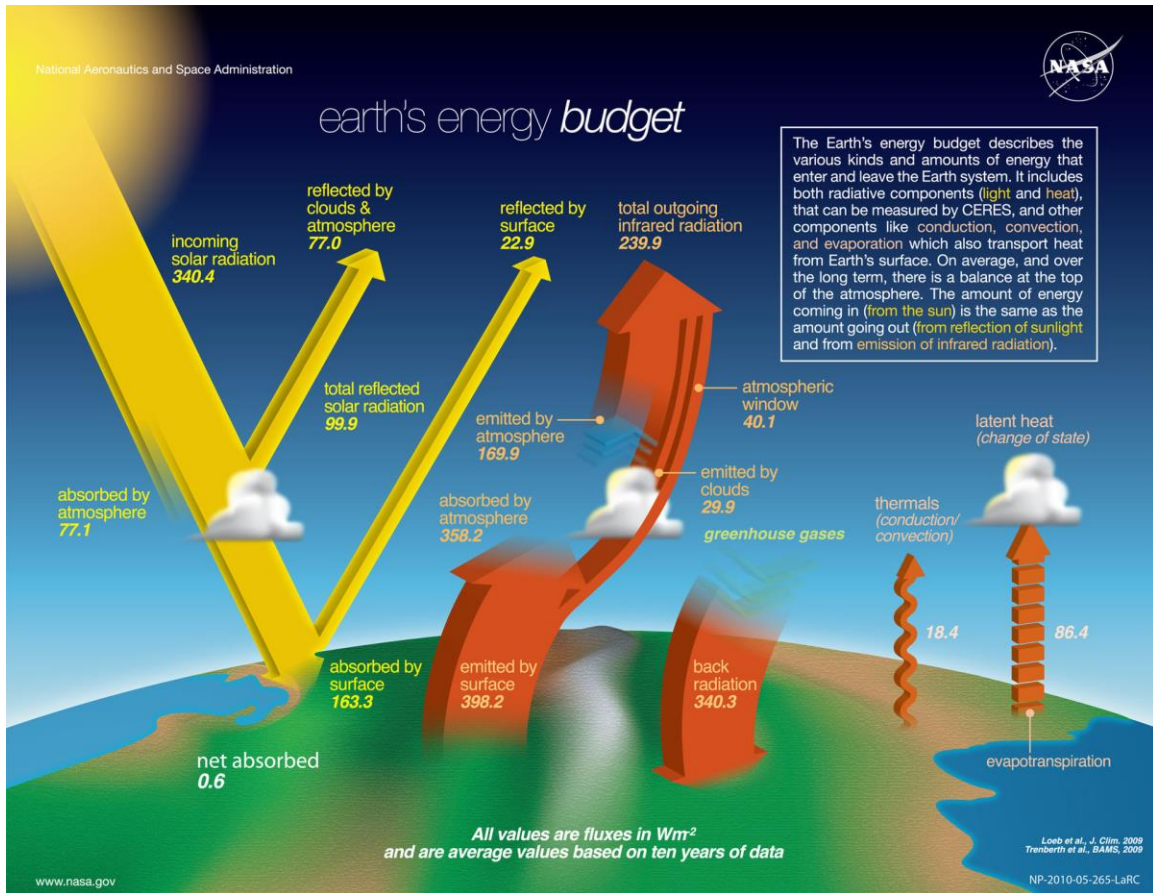


Figure 1. Image. Earth's energy balance system. (NASA 2014)

RADIATION MODELS USED IN PMED ANALYSES

The PMED software models these radiation energy components based on weather characteristics (i.e., hourly air temperature, percent sunshine, wind speed, precipitation, and relative humidity) and pavement characteristics (i.e., surface shortwave absorptivity, emissivity, surface temperature, thermal conductivity, and heat capacity). Previous studies have quantified the sensitivity of predicted pavement performance to many of these inputs, identified various issues with the quality of the original climate data provided with the PMED software, and explored alternative climate data sources; these previous studies were documented in Phase I of GDOT RP 16-10 (Durham et al. 2019).

PMED estimates the net SWR based on empirical relationships, as shown in equation 1 (Dempsey et al. 1985).

$$Q_s = a_s * R * (A + \frac{BS_c}{100}) \quad (1)$$

where, Q_s is net shortwave radiation; a_s is surface shortwave absorptivity of the pavement surface; R is extraterrestrial radiation incident at the top of the atmosphere; A, B are diffuse scattering and adsorption coefficients; and S_c is percent sunshine.

The primary PMED climate modeling deficiency addressed in Phase I of GDOT RP 16-10 (Durham et al. 2019) was the indirect computation of SWR using percent sunshine and other empirical relations (equation 1). The Phase I work proposed and validated improvements to SWR modeling and made suggestions for the enhancement of the PMED software. Equation 1 has empirical constants (A and B) that were calibrated for northern-tier states in the United States and Canada. Therefore, these constants do not represent the entirety of the U.S. In addition, the percent sunshine, defined as “100 percent cloud cover,” is poorly defined/measured and complicated by the fact that different cloud types have different SWR absorption characteristics (Várnai and Davies 1999). That is, even though cloud cover may be 100 percent, optically-thin versus optically-thick clouds bear a significant influence on the amount of SWR that reaches the pavement surface. The recommendation of Phase I of GDOT RP 16-10 (Durham et al. 2019) was to utilize the direct SWR estimates of MERRA-2 for more accurate, physics-based, and reliable inputs for use in PMED design in the future.

In PMED analyses, the presence of clouds reduces D-LWR whereas first-order physical principles prove that clouds, in reality, serve to amplify D-LWR at the pavement

surface. The D-LWR for a clear-sky condition can be determined based on the relationships as shown in equation 2 (Unsworth 1975).

$$Q_z = \sigma_{sb} * \epsilon * T_{air}^4 \quad (2)$$

where, Q_z is downwelling longwave radiation without cloud cover correction, σ_{sb} is the Stefan–Boltzmann constant, ϵ is atmospheric emissivity, and T_{air} is air temperature.

PMED follows Dempsey et al. (1985) parameterization to analyze the atmospheric emissivity, as shown in equation 3.

$$\epsilon_D = \left(G - \frac{J}{10\rho p} \right) \quad (3)$$

where, ϵ_D is atmospheric emissivity parameterization proposed by Dempsey et al. (1985); G, J, ρ are regression coefficients; and p is vapor pressure of air (1 to 10 mm Hg)

Hourly D-LWR data as required by the EICM are not available in any atmospheric data reanalysis program databases, including MERRA-2. However, the atmospheric emissivity can be estimated based on different alternative parameterizations. Equations 4, 5, and 6 illustrate the atmospheric emissivity parameterizations proposed by Ångström (1915), Idso (1981), and Brunt (1932), respectively (Forman and Margulis 2009).

$$\epsilon_A = a_A - b_A * 10^{-c_A p} \quad (4)$$

$$\epsilon_I = a_I + b_I * p \quad (5)$$

$$\epsilon_B = a_B + b_B \sqrt{p} \quad (6)$$

where, $\epsilon_A, \epsilon_I, \epsilon_B$ are atmospheric emissivity parameterizations proposed by Ångström (1915), Idso (1981), and Brunt (1932), respectively; a_A, b_A, c_A are regression coefficients proposed by Ångström (1915); a_I, b_I are regression coefficients proposed by Idso (1981); a_B, b_B are regression coefficients proposed by Brunt (1932); and p is vapor pressure of air (1 to 10 mm Hg)

PMED determines the D-LWR for the all-sky condition, as shown in equation 7 (Dempsey et al. 1985).

$$Q_a = Q_z * (1 - \frac{N_D W}{100}) \quad (7)$$

where, Q_a is downwelling longwave radiation with cloud cover correction, Q_z is downwelling longwave radiation without cloud cover correction, N_D (= 0.8 to 0.9) is cloud base factor proposed by Dempsey et al. (1985), and W is cloud cover.

Cloud cover effects (equation 7) appear to be in the wrong direction. Cloud cover—especially warm clouds at low altitudes—should increase net LWR, not decrease it. Assuming air temperature is held constant, the presence of clouds increases the amount of precipitable water that, in general, increases the emissivity of the atmosphere, which in turn amplifies the amount of D-LWR that reaches the pavement surface (Forman and Margulis 2010; Sugita and Brutsaert 1993). If clouds are located high in the troposphere (e.g., ~10 km), the effect on D-LWR at the pavement surface is minimal. Therefore, clouds serve to amplify D-LWR, or in the case of thin cirrus clouds, e.g., do little to modulate D-LWR at the pavement surface. However, the PMED-recommended D-LWR model systematically attenuates the D-LWR in a manner that is inconsistent with most radiative transfer models. A more physically consistent parameterization to estimate for D-LWR based on cloud amplification factor is shown in equation 8 (Iziomon et al. 2003; Sugita and Brutsaert 1993).

$$Q_a = Q_z * (1 + \frac{N W}{100}) \quad (8)$$

where, Q_a is downwelling longwave radiation with cloud cover correction, Q_z is downwelling longwave radiation without cloud cover correction, N (= 0.17) is cloud amplification factor, and W is cloud cover.

The PMED-recommended U-LWR for clear and all-sky conditions are shown in equations 9 and 10, respectively (Dempsey et al. 1985).

$$Q_x = \sigma_{sb} * \epsilon * T_s^4 \quad (9)$$

$$Q_e = Q_x * (1 - \frac{N_D W}{100}) \quad (10)$$

where, Q_x is upwelling longwave radiation without cloud cover correction, Q_e is upwelling longwave radiation with cloud cover correction, ϵ is emissivity of the pavement, T_s is surface temperature, N_D (= 0.8 to 0.9) is cloud base factor proposed by Dempsey et al. (1985), W is cloud cover, and σ_{sb} is the Stefan–Boltzmann constant.

The U-LWR appears to be influenced by the cloud cover (equation 10). However, the presence of cloud cannot influence the radiation emission from the pavement surface to the atmosphere (Koll and Cronin 2018). Thereby, a more physically consistent parameterization for U-LWR under the all-sky condition should be equal to the U-LWR under the clear-sky condition; as shown in equation 11.

$$Q_e = Q_x = \sigma_{sb} * \epsilon * T_s^4 \quad (11)$$

where, Q_x is upwelling longwave radiation without cloud cover correction, Q_e is upwelling longwave radiation with cloud cover correction, ϵ is emissivity of the pavement, T_s is surface temperature, and σ_{sb} is the Stefan–Boltzmann constant.

CHAPTER 3. RESEARCH METHODOLOGY

EVALUATION OF SHORTWAVE AND LONGWAVE RADIATION MODELS

Ground-based stations are utilized to compare D-LWR models as well as D-SWR estimates collected from MERRA-2. Radiation observations from solar infrared radiation stations (SIRSs), operated by the Department of Energy's program for Atmospheric Radiation Measurement (ARM; <https://www.arm.gov/capabilities/instruments/sirs>), are used as ground truth radiation data. Unlike D-SWR observations, which are publicly available across the country, the availability of D-LWR observations is much more limited. The SIRS LWR radiometers are probably the only multi-year, publicly-available D-LWR observations available for such a comparison. An extensive quality control procedure—both automated and by visual inspection—was made for all of the observations used in this study to ensure an appropriate comparison in both space and time between the ground-based SIRS observations and the model-based reanalysis estimates. The SIRS observations are point-scale (figure 2). On the other hand, the MERRA-2 atmospheric reanalysis products are provided at a model grid cell-scale. However, these scale differences are minimized in the relatively flat and homogeneous terrain. Comparison against SIRS measurements provides useful guidance as to the quality of the model results and can help identify systematic errors. The original SIRS observations are provided as 5-minute averages but have been upscaled in time to 1 hour. All subsequent comparisons presented here are made at the hourly timescale and are conducted over a period of approximately 18 years (i.e., from January 01, 2002, to the near-present). The hourly upscaling is necessary because the MERRA-2 inputs used in the model-based (reanalysis) estimates are provided at an hourly timescale.

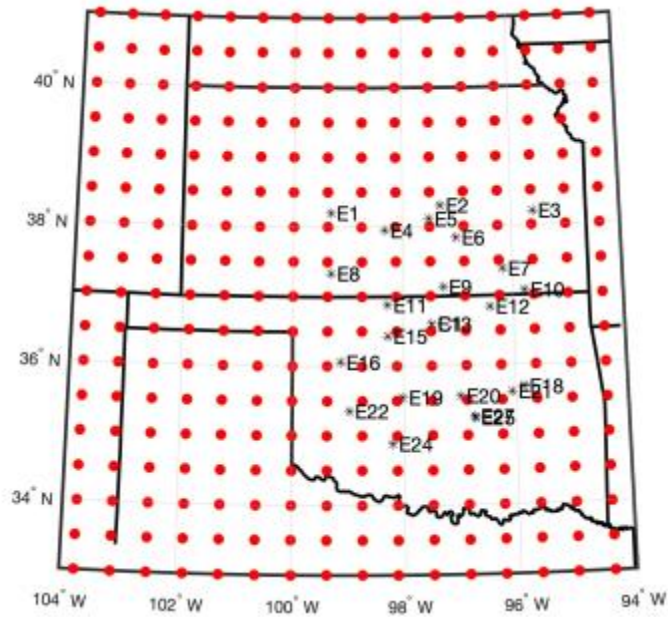


Figure 2. Image. Locations of the SIRS stations (black dots) used in the analysis. (Red dots refer to the MERRA-2 grid cells.)

SHORTWAVE AND LONGWAVE RADIATION MODELS USED IN PAVEMENT DISTRESS ANALYSES

The impacts of seven different cases of shortwave and longwave radiation models on AC pavement distress responses are assessed. Descriptions for each case are as follows.

- **Case 1:** The PMED-recommended models were used without any modification.
- **Case 2:** The hourly D-SWR obtained from MERRA-2 were used to determine the net SWR as shown in equation 12 (Dempsey et al. 1985).

$$Q_s = a_s * Q_i \quad (12)$$

where, Q_s is net SWR, a_s is surface shortwave absorptivity of the pavement surface ($a_s = 1 - Albedo$), and Q_i is the downwelling SWR that is a product of the MERRA-2 reanalysis.

- **Case 3:** The case 2 model was further updated to calculate atmospheric emissivity using the Idso (1981) parameterization (equation 5) and the D-LWR for the all-sky condition using the cloud amplification factor (equation 8).
- **Case 4:** The case 2 model was further updated to model U-LWR using a more physically consistent parameterization (equation 12).
- **Case 5:** Both the D-LWR and U-LWR models were updated, along with the SWR updates outlined in case 2. Atmospheric emissivity was calculated with the Idso (1981) parameterization (equation 5). Then, the subsequent D-LWR during the all-sky condition was analyzed using a physically consistent cloud amplification factor (equation 8). A more physically consistent parameterization was followed to model U-LWR (equation 12).
- **Case 6:** The case 2 model was further updated to calculate atmospheric emissivity using the Idso (1981) parameterization (equation 5.) The D-LWR during the all-sky condition was determined using the cloud amplification factor (equation 8). Hourly-averaged vapor pressure data computed using inputs from MERRA-2 were utilized to calculate atmospheric emissivity.
- **Case 7:** Cases 5 and 7 were identical except for the atmospheric emissivity calculation (equation 5). In case 5, a constant vapor pressure of 10 mm Hg was assumed, as in the PMED software. This assumption was based on the Dempsey et al. (1985) parameterization. In case 7, hourly-averaged vapor pressure data were computed using inputs from MERRA-2. Then, the dynamic, hourly-averaged vapor pressure was used to compute atmospheric emissivity. Vapor pressure often undergoes large, subdiurnal variations, which can be significant

in subtropical regions such as Georgia (Anderson 1936). One of the objectives in cases 5 and 7 was to assess the pavement responses for constant versus dynamic vapor pressure. This comparison helps identify the significance of the vapor pressure response on the pavement distress predictions.

Pavement distresses predicted via case 1 (unmodified PMED method), case 2 (modified D-SWR), case 5 (modified LWR), and case 7 (modified LWR with dynamic vapor pressure) are highlighted in CHAPTER 4. RESULTS Among these, analysis case 7 represents the most accurate radiation models. Analysis cases 3, 4, and 6 are hypothetical cases that were defined to observe the unit response of pavement distresses due to updates in each radiation model.

MECHANISTIC–EMPIRICAL ASPHALT PAVEMENT ANALYSIS

The source code of PMED is not publicly available. As a result, these different analysis cases cannot be directly implemented into the EICM module. Therefore, a flexible pavement design and analysis software called Mechanistic–Empirical Asphalt Pavement Analysis (MEAPA) (<https://paveapps.com/meapa/>) was used to simulate these analyses. MEAPA was developed based on the MEPDG documentation and uses similar pavement response, transfer function, and distress models as implemented in the MEPDG. Unlike PMED, however, MEAPA provides access to the program source code. Therefore, analysis cases 1 through 7 based on the different shortwave and longwave radiation models can be simulated in MEAPA. The MEAPA-simulated pavement responses help provide insight into the impacts of the various shortwave and longwave radiation models on AC pavement distresses. Total rutting (TR), AC layer rutting (AR), and bottom-up fatigue cracking

(BUFC) pavement distresses were investigated. All analyses use the PMED global field calibration factor.

DESIGN INPUTS USED TO ANALYZE PAVEMENT DISTRESSES

Five MERRA-2 stations were selected in Georgia and Alabama for pavement distress analyses. The geo-coordinates and elevations of the corresponding MERRA-2 cell centers are shown in figure 3 and table 1. Typical GDOT PMED design inputs were used for MEAPA simulations. Table 2 summarizes the traffic level and the thicknesses of the pavement layers. Table 3 and table 4 summarize the other major inputs used in the MEAPA simulations.

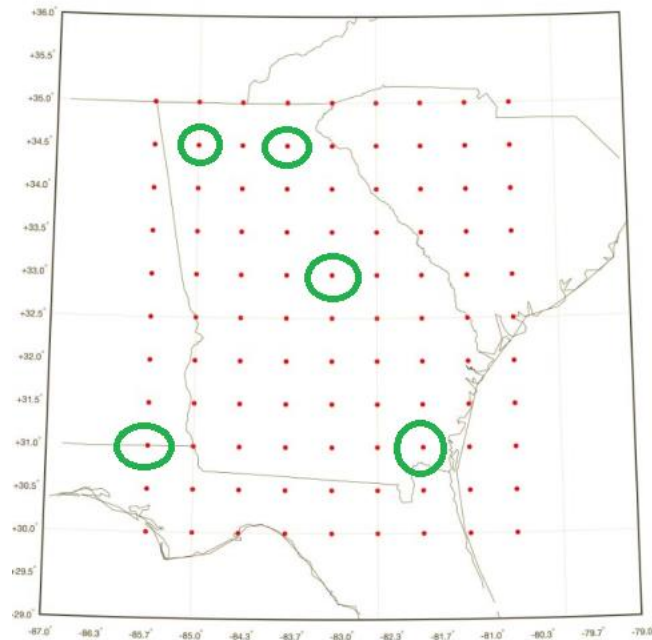


Figure 3. Image. Locations of the test locations (green circles) used in the regional analysis. (Red dots refer to the MERRA-2 grid cells.)

Table 1. Summary of the MERRA-2 stations used in the analyses.

Climate Station Site ID	Latitude (degrees)	Longitude (degrees)	Elevations (m)
133789	31.000	-82.500	42.980
134360	31.500	-85.625	128.970
136092	33.000	-83.125	70.980
137817	34.500	-85.000	200.950
137819	34.500	-83.750	430.890

Table 2. Traffic and AC pavement layer thicknesses.

Nominal AADTT*	4,000
AC thickness (cm)	18.5
Base thickness (cm)	25.4
Subbase thickness (cm)	25.4

*Annual average daily truck traffic

Table 3. AC pavement design properties.

Design life	20 years
Reliability	50%
Number of lanes in design direction	2
Truck direction factor	50%
Truck lane factor	95%
Growth rate	3%
Growth function	Linear
Surface layer material type	Asphalt concrete
Base layer material type	Nonstabilized base (crushed stone)
Base layer resilient modulus	158,580 kPa
Base layer Poisson's ratio	0.35
Subbase layer material type	Nonstabilized sub base (A-1-b)
Subbase layer resilient modulus	124,106 kPa
Subbase layer Poisson's ratio	0.35
Subgrade layer material type	A-6
Subgrade layer resilient modulus	96,527 kPa
Subgrade layer Poisson's ratio	0.35

Table 4. AC surface layer properties.

Surface shortwave absorptivity	0.85
Unit weight (kg/m ³)	2,370.73
Poisson's ratio	0.35
Thermal conductivity (Wm ⁻¹ K ⁻¹)	1.157
Heat capacity (Wm ⁻¹ K ⁻¹)	0.266
Effective binder content (%)	10.5
Air void (%)	6

CHAPTER 4. RESULTS

EVALUATION OF DOWNWELLING SHORTWAVE RADIATION MODEL

In this study, MERRA-2 D-SWR estimates are compared against the ground-based radiometer observations collected from SIRS (figure 4). The D-SWR estimates from the MERRA-2 reanalysis are in excellent agreement with the SIRS observations. This is further confirmation, in addition to the results of Cetin et al. (2018), Durham et al. (2019), and Schwartz et al. (2015), of the ability of MERRA-1 and MERRA-2 to accurately estimate D-SWR flux at the land surface during all times of the day and all times of the year. The one exception of D-SWR flux estimation performance is in the presence of small-scale clouds (e.g., convective systems common during the summer), where MERRA-2 has a tendency to overestimate D-SWR flux as compared to SIRS. This is because small-scale convective clouds on the order of a few square kilometers are effectively “smoothed” out in MERRA-2, which is at the scale of ~50 km by ~65 km, that in turn underestimates the cloud optical thickness. The result is less attenuation in MERRA-2 D-SWR estimates, thereby allowing more D-SWR radiation to reach the land surface as compared to that measured by SIRS. However, in the context of pavement modeling, these situations (i.e., when the D-SWR fluxes are relatively small due to cloud attenuation) are relatively benign because it is the occurrence of large amounts of SWR radiation (e.g., clear-sky conditions during the summer) which serve to heat of the pavement surface the most, and as a result, have the greatest impact on the pavement temperature, rutting, and other deleterious effects to the pavement surface.

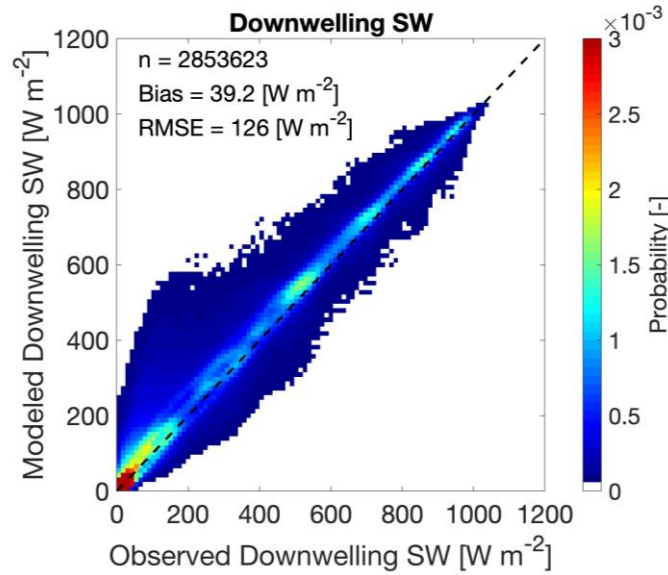


Figure 4. Graph. Probability plots of calculated D-SWR values based on MERRA-2 against the SIRS observations of D-SWR.

EVALUATION OF DOWNWELLING LONGWAVE RADIATION MODEL

D-LWR based on the Dempsey et al. (1985) model are compared with SIRS observations (figure 5). Figure 5(a) presents results that assume the absence of clouds (i.e., emitted downwelling radiation by the near-surface atmosphere only). The results illustrate a large negative bias (bias = -58.6 W m^{-2}) in the form of systematic error, along with a moderate amount of systematic plus random error (root mean square error [RMSE] = 65.5 W m^{-2}). The cloud effects are then included in figure 5(b) and illustrate both the atmospheric and cloud portions that contributed to the total D-LWR radiation at the land surface during all-sky conditions. When the effects of clouds are introduced, the deleterious effects of the improper model physics are evident. As seen in figure 5(b), the LWR bias becomes more negative (bias = -123 W m^{-2}) as the RMSE correspondingly increases (RMSE = 156 W m^{-2}). These results clearly show how the parameterization of Dempsey et al. (1985) improperly accounts for cloud amplification of D-LWR flux at the land surface.

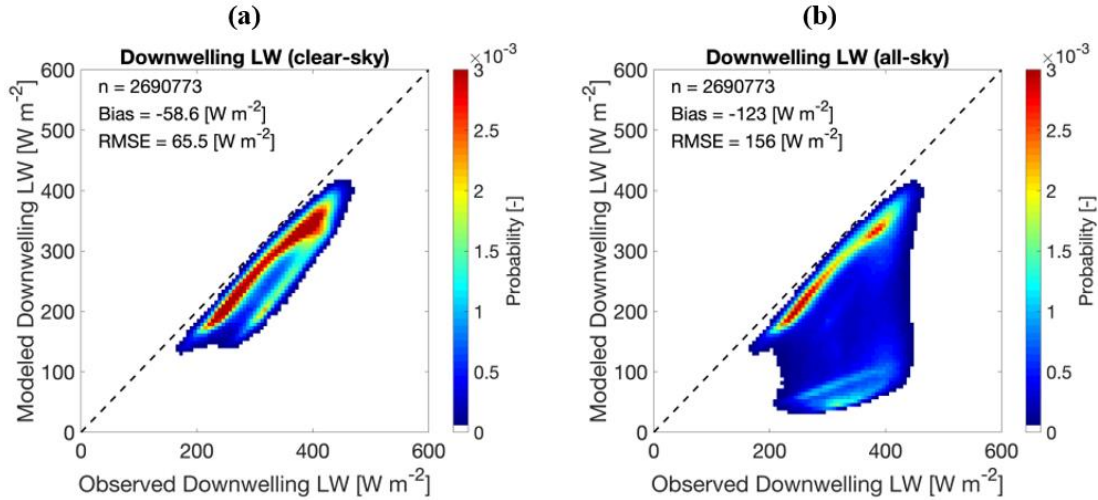


Figure 5. Graphs. Probability plots of observed and modeled radiation fluxes for (a) D-LWR flux assuming clear-sky conditions, and (b) D-LWR flux during all-sky conditions including cloud amplification. (D-LWR results are based on Dempsey et al. [1985].)

D-LWR based on the Ångström (1915) model are compared with SIRS observations (figure 6). As shown in figure 6(a), the clear-sky parameterization from Ångström (1915) improves the results via a reduction of bias (bias = -21.4 W m^{-2}), along with a reduction in RMSE (RMSE = 37.3 W m^{-2}). These results suggest the atmospheric emissivity in Ångström (1915) is more applicable in the Southern Great Plains than that of Dempsey et al. (1985). As seen in figure 6(b), the alternative cloud parameterization further improves the LWR results by accounting for cloud amplification rather than cloud attenuation of D-LWR. Namely, the bias is further reduced (bias = -5.8 W m^{-2}), as is the RMSE (RMSE = 29.8 W m^{-2}). These results corroborate the results in figure 6, where clouds serve to amplify D-LWR rather than attenuate D-LWR according to Dempsey et al. (1985).

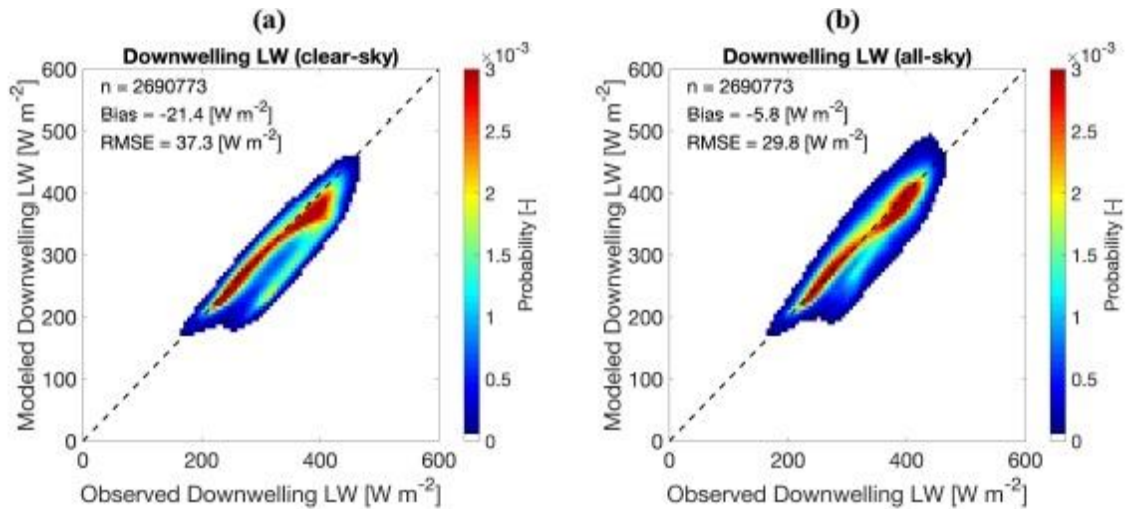


Figure 6. Graphs. Probability plots of observed and modeled radiation fluxes for (a) D-LWR flux assuming clear-sky conditions; and (b) D-LWR flux during all-sky conditions, including cloud amplification. (D-LWR results are based on Ångström [1915].)

D-LWR based on the Brunt (1932) model are compared with SIRS observations (figure 7). The clear-sky parameterization according to Brunt (1932) in figure 7(a) also improves the results relative to Dempsey et al. (1985) via a reduction of bias (bias = -25.8 W m^{-2}), along with a reduction in RMSE (RMSE = 41.4 W m^{-2}). These results suggest the atmospheric emissivity in Brunt (1932) is more applicable in the Southern Great Plains than that of Dempsey et al. (1985). Moreover, as seen in figure 7(b), the alternative cloud parameterization further improves the results by accounting for cloud amplification rather than cloud attenuation of D-LWR. Namely, the bias is further reduced (bias = -10.4 W m^{-2}), as is the RMSE (RMSE = 34.4 W m^{-2}). These results corroborate the results in figure 5, where clouds serve to amplify D-LWR rather than attenuate D-LWR according to Dempsey et al. (1985).

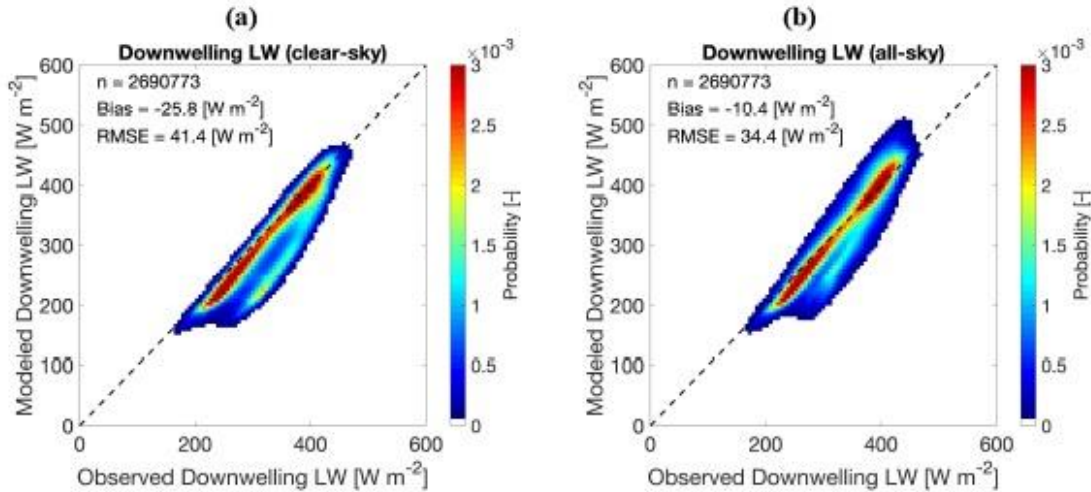


Figure 7. Graphs. Probability plots of observed and modeled radiation fluxes for (a) D-LWR flux assuming clear-sky conditions; and (b) D-LWR flux during all-sky conditions, including cloud amplification. (D-LWR results are based on Brunt [1932].)

D-LWR based on the Idso (1981) model are compared with SIRS observations (figure 8). The clear-sky parameterization according to Idso (1981) in figure 8(a) yields the greatest improvements relative to Dempsey et al. (1985) via a reduction of bias (bias = -15.3 W m^{-2}), along with a reduction in RMSE (RMSE = 34.2 W m^{-2}). These results suggest the atmospheric emissivity in Idso (1981) is more applicable in the Southern Great Plains than that of Dempsey et al. (1985). As seen in figure 8(b), the alternative cloud parameterization further improves the results by accounting for cloud amplification rather than cloud attenuation of D-LWR. Namely, the bias is reduced to near zero (bias = -0.589 W m^{-2}) with a corresponding improvement to RMSE (RMSE = 29.5 W m^{-2}).

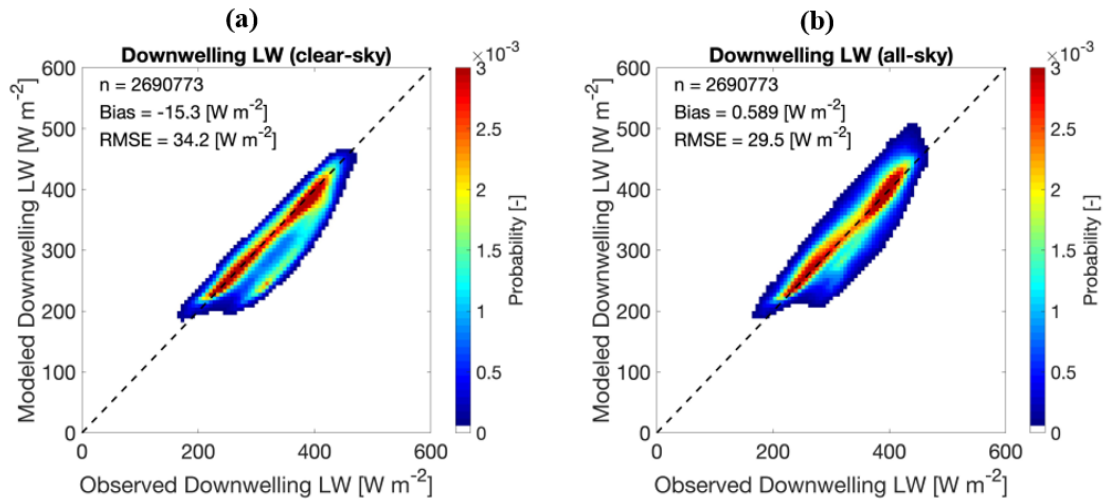


Figure 8. Graphs. Probability plots of observed and modeled radiation fluxes for (a) D-LWR flux assuming clear-sky conditions; and (b) D-LWR flux during all-sky conditions, including cloud amplification effects. (D-LWR results are based on Idso [1981].)

The fundamental physics of D-LWR emission suggest clouds serve to amplify D-LWR at the land surface due to an increase in emissivity associated with an increase in total atmospheric water content (a.k.a., precipitable water), assuming the atmospheric temperature is held constant. The results presented here have clearly demonstrated how accounting for cloud amplification (rather than cloud attenuation) vastly improves LWR estimates relative to the parameterization presented in Dempsey et al. (1985). Of the three different LWR parameterizations explored during this study, the method of Idso (1981) outperformed that of Dempsey et al. (1985) the most during both clear-sky and all-sky conditions with a near-zero bias and a minimized amount of systematic and random error. It is therefore suggested that the LWR parameterization be updated from Dempsey et al. (1985) to Idso (1981) when modeling downwelling LWR at the land surface in the context of pavement performance.

IMPACTS OF THE SHORTWAVE AND LONGWAVE RADIATION MODELS IN PAVEMENT DISTRESSES AND TEMPERATURE PROFILES PREDICTIONS

The pavement distresses and surface temperature predictions are compared for analysis cases 1 through 7 (figure 9 to Figure 28). These analyses use the PMED-recommended global field calibration factors. For all modified methods (cases 2 to 7), the pavement responses were significantly impacted compared to those obtained using the unmodified method (case 1). Pavement distresses and average surface temperature predictions were significantly higher for analysis case 7, which represents the most accurate radiation models, compared to those predictions from case 1 (unmodified PMED method). Detailed results of total rutting, asphalt layer rutting, bottom-up fatigue cracking, and average pavement temperature predictions for all five climatic locations are provided in this chapter. A summary of these results and discussions is presented in chapter 5.

Total Rutting Predictions

The impacts of the shortwave and longwave radiation models on the total rutting prediction are shown in figure 9 for the city of Clayton, Georgia. For case 1 (unmodified PMED), the TR estimate was 0.22 inch. When the shortwave radiation model was updated (case 2), the TR estimate increased to 0.33 inch. After the D-LWR model was modified (case 3), the TR estimate increased to 0.50 inch. As a result of changing the U-LWR model (case 4), the TR estimate decreased to 0.18 inch. When the both U-LWR and D-LWR models were updated with constant-value vapor pressure data (case 5), the TR estimate increased to 0.40 inch. After the D-LWR model was updated with dynamic vapor pressure data (case 6), the TR estimate increased to 0.53 inch. Finally, as a result of using the U-LWR and D-LWR models with dynamic vapor pressure data (case 7), the TR estimate was 0.40 inch.

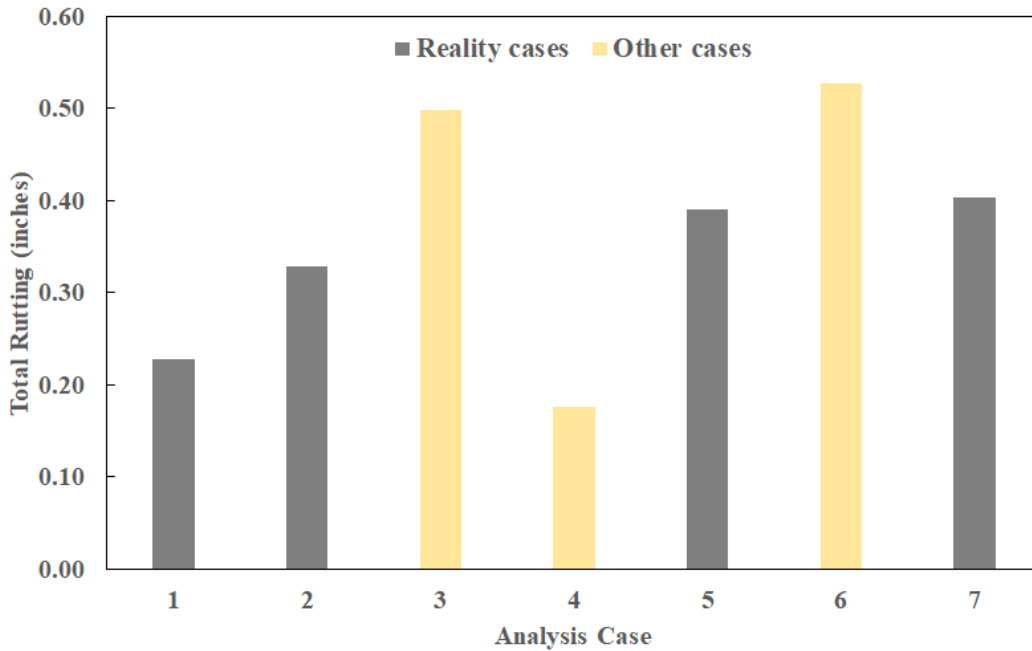


Figure 9. Graph. Impacts of radiation models on total rutting prediction in Clayton, GA.

The impacts of the shortwave and longwave radiation models on the total rutting prediction are shown in figure 10 for the city of Donalsonville, Georgia. For case 1 (unmodified PMED) the TR estimate was 0.23 inch. When the shortwave radiation model was updated (case 2), the TR estimate increased to 0.30 inch. After the D-LWR model was modified (case 3), the TR estimate increased to 0.44 inch. As a result of changing the U-LWR model (case 4), the TR estimate decreased to 0.18 inch. When both the U-LWR and D-LWR models were updated with constant-value vapor pressure data (case 5), the TR estimate increased to 0.36 inch. After the D-LWR model was updated with dynamic vapor pressure data (case 6), the TR estimate increased to 0.47 inch. Finally, as a result of using the U-LWR and D-LWR models with dynamic vapor pressure data (case 7), the TR estimate was 0.38 inch.

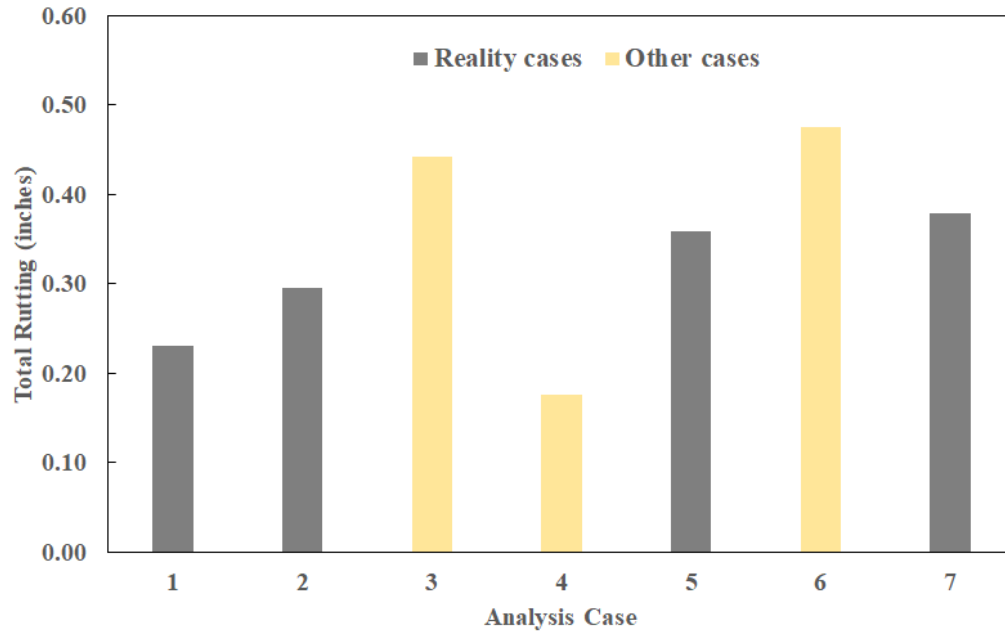


Figure 10. Graph. Impacts of radiation models on total rutting prediction in Donalsonville, GA.

The impacts of the shortwave and longwave radiation models on the total rutting prediction are shown in figure 11 for the city of Jeffersonville, Georgia. For case 1 (unmodified PMED), the TR estimate was 0.23 inch. When the shortwave radiation model was updated (case 2), the TR estimate increased to 0.29 inch. After the D-LWR model was modified (case 3), the TR estimate increased to 0.42 inch. As a result of changing the U-LWR model (case 4), the TR estimate decreased to 0.18 inch. When both the U-LWR and D-LWR models were updated with constant-value vapor pressure data (case 5), the TR estimate increased to 0.35 inch. After the D-LWR model was updated with dynamic vapor pressure data (case 6), the TR estimate increased to 0.45 inch. Finally, as a result of using the U-LWR and D-LWR models with dynamic vapor pressure data (case 7), the TR estimate was 0.36 inch.



Figure 11. Graph. Impacts of radiation models on total rutting prediction in Jeffersonville, GA.

The impacts of the shortwave and longwave radiation models on the total rutting prediction are shown in figure 12 for the city of Trenton, Georgia. For case 1 (unmodified PMED), the TR estimate was 0.23 inch. When the shortwave radiation model was updated (case 2), the TR estimate increased to 0.33 inch. After the D-LWR model was modified (case 3), the TR estimate increased to 0.53 inch. As a result of changing the U-LWR model (case 4), the TR estimate decreased to 0.18 inch. When both the U-LWR and D-LWR models were updated with constant-value vapor pressure data (case 5), the TR estimate increased to 0.41 inch. After the D-LWR model was updated with dynamic vapor pressure data (case 6), the TR estimate increased to 0.56 inch. Finally, as a result of using the U-LWR and D-LWR models with dynamic vapor pressure data (case 7), the TR estimate was 0.43 inch.

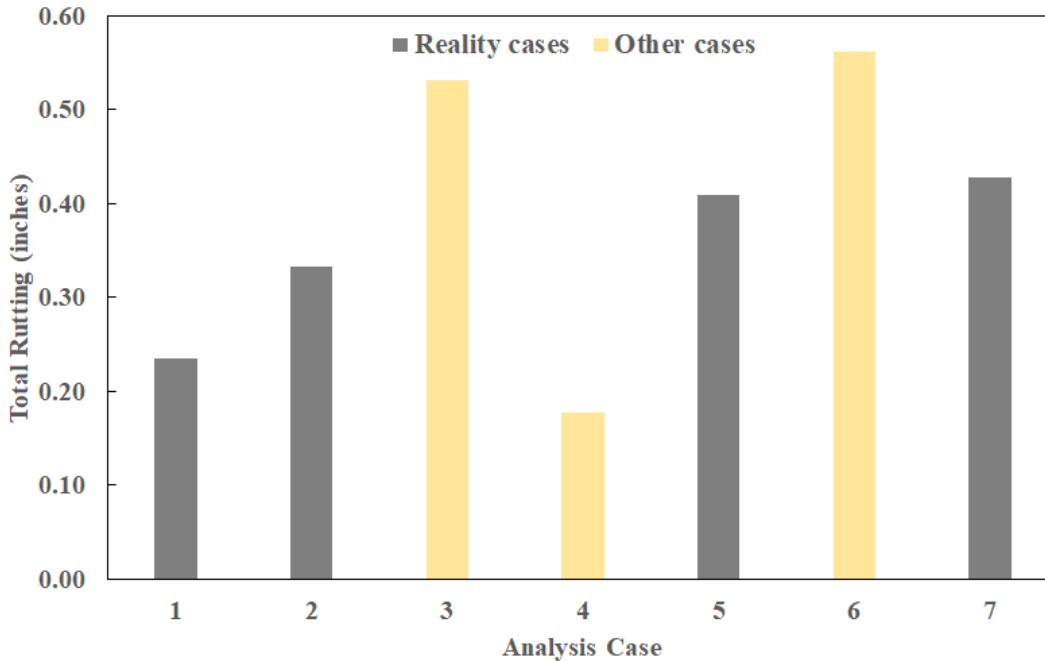


Figure 12. Graph. Impacts of radiation models on total rutting prediction in Trenton, GA.

The impacts of the shortwave and longwave radiation models on the total rutting prediction are shown in **Error! Reference source not found.** for the city of Woodbine, Georgia. For case 1 (unmodified PMED), the TR estimate was 0.22 inch. When the shortwave radiation model was updated (case 2), the TR estimate increased to 0.27 inch. After the D-LWR model was modified (case 3), the TR estimate increased to 0.37 inch. As a result of changing the U-LWR model (case 4), the TR estimate decreased to 0.18 inch. When both the U-LWR and D-LWR models were updated with constant-value vapor pressure data (case 5), the TR estimate increased to 0.31 inch. After the D-LWR model was updated with dynamic vapor pressure data (case 6), the TR estimate increased to 0.40 inch. Finally, as a result of using the U-LWR and D-LWR models with dynamic vapor pressure data (case 7), the TR estimate was 0.33 inch.

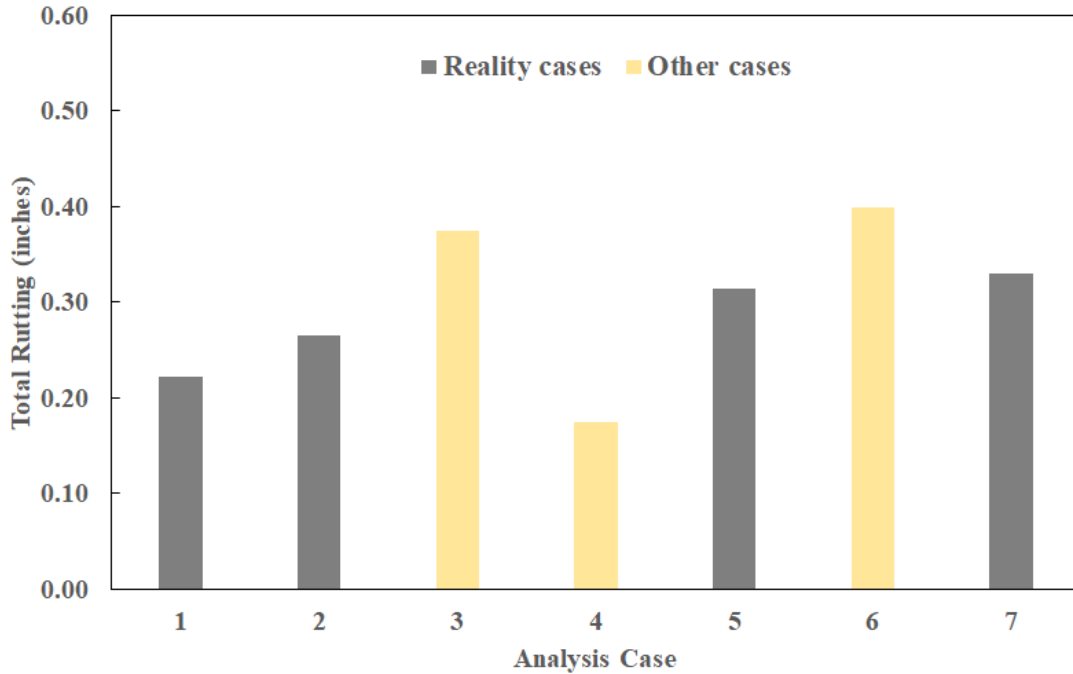


Figure 13. Graph. Impacts of radiation models on total rutting prediction in Woodbine, GA.

Asphalt Layer Rutting Predictions

The impacts of the shortwave and longwave radiation models on the asphalt layer rutting prediction are shown in **Error! Reference source not found.**for the city of Clayton, Georgia. For case 1 (unmodified PMED), the AR estimate was 0.07 inch. When the shortwave radiation model was updated (case 2), the AR estimate increased to 0.17 inch. After the D-LWR model was modified (case 3), the AR estimate increased to 0.33 inch. As a result of changing the U-LWR model (case 4), the AR estimate decreased to 0.03 inch. When both the U-LWR and D-LWR models were updated with constant-value vapor pressure data (case 5), the AR estimate increased to 0.22 inch. After the D-LWR model was updated with dynamic vapor pressure data (case 6), the AR estimate increased to

0.36 inch. Finally, as a result of using the U-LWR and D-LWR models with dynamic vapor pressure data (case 7), the AR estimate was 0.24 inch.

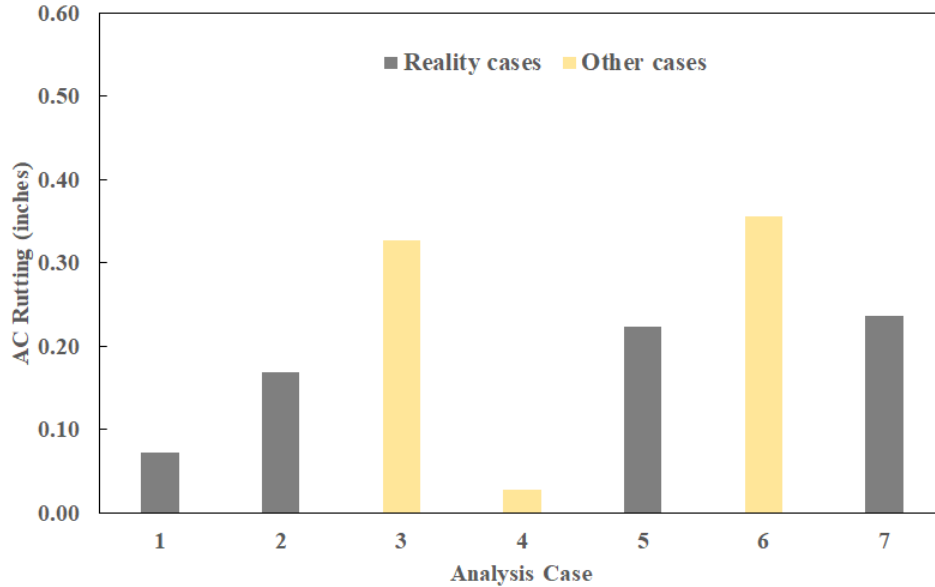


Figure 14. Graph. Impacts of radiation models on asphalt layer rutting prediction in Clayton, GA.

The impacts of the shortwave and longwave radiation models on the asphalt layer rutting prediction are shown in figure 15 for the city of Donalsonville, Georgia. For case 1 (unmodified PMED), the AR estimate was 0.07 inch. When the shortwave radiation model was updated (case 2), the AR estimate increased to 0.13 inch. After the D-LWR model was modified (case 3), the AR estimate increased to 0.27 inch. As a result of changing the U-LWR model (case 4), the AR estimate decreased to 0.03 inch. When both the U-LWR and D-LWR models were updated with constant-value vapor pressure data (case 5), the AR estimate increased to 0.19 inch. After the D-LWR model was updated with dynamic vapor pressure data (case 6), the AR estimate increased to 0.30 inch. Finally, as a result of

using the U-LWR and D-LWR models with dynamic vapor pressure data (case 7), the AR estimate was 0.21 inch.



Figure 15. Graph. Impacts of radiation models on asphalt layer rutting prediction in Donalsonville, GA.

The impacts of the shortwave and longwave radiation models on the asphalt layer rutting prediction are shown in figure 16 for the city of Jeffersonville, Georgia. For case 1 (unmodified PMED), the AR estimate was 0.07 inch. When the shortwave radiation model was updated (case 2), the AR estimate increased to 0.13 inch. After the D-LWR model was modified (case 3), the AR estimate increased to 0.25 inch. As a result of changing the U-LWR model (case 4), the AR estimate decreased to 0.03 inch. When both the U-LWR and D-LWR models were updated with constant-value vapor pressure data (case 5), the AR estimate increased to 0.18 inch. After the D-LWR model was updated with dynamic vapor pressure data (case 6), the AR estimate increased to 0.28 inch. Finally, as a result of

using the U-LWR and D-LWR models with dynamic vapor pressure data (case 7), the AR estimate was 0.20 inch.



Figure 16. Graph. Impacts of radiation models on asphalt layer rutting prediction in Jeffersonville, GA.

The impacts of the shortwave and longwave radiation models on the asphalt layer rutting prediction are shown in figure 17 for the city of Trenton, Georgia. For case 1 (unmodified PMED), the AR estimate was 0.08 inch. When the shortwave radiation model was updated (case 2), the AR estimate increased to 0.17 inch. After the D-LWR model was modified (case 3), the AR estimate increased to 0.36 inch. As a result of changing the U-LWR model (case 4), the AR estimate decreased to 0.03 inch. When both the U-LWR and D-LWR models were updated with constant-value vapor pressure data (case 5), the AR estimate increased to 0.24 inch. After the D-LWR model was updated with dynamic vapor pressure data (case 6), the AR estimate increased to 0.39 inch. Finally, as a result of

using the U-LWR and D-LWR models with dynamic vapor pressure data (case 7), the AR estimate was 0.26 inch.

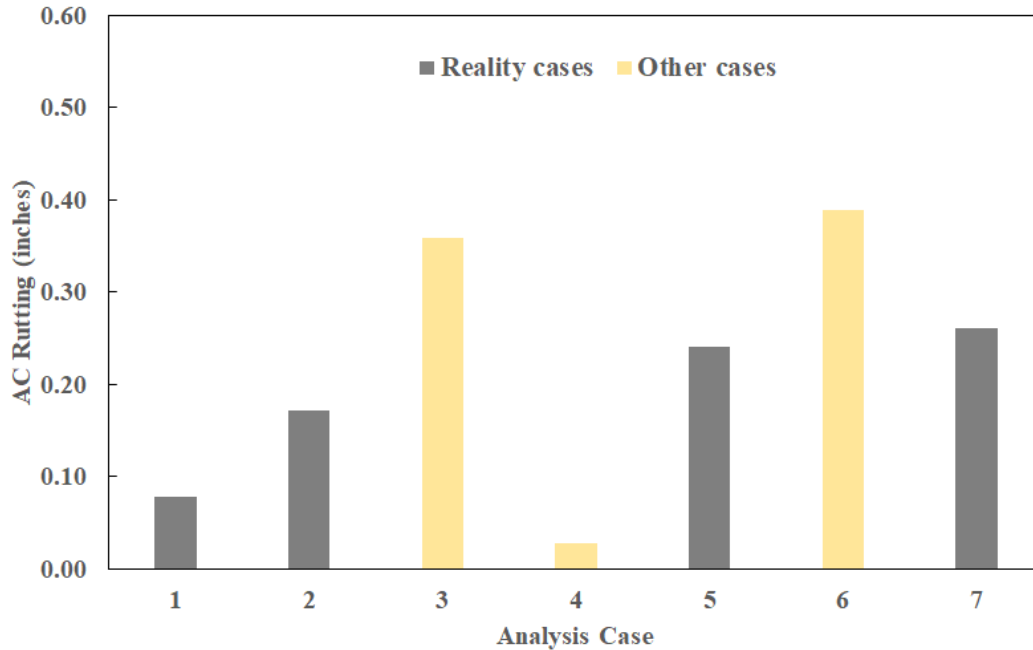


Figure 17. Graph. Impacts of radiation models in asphalt layer rutting prediction in Trenton, GA.

The impacts of the shortwave and longwave radiation models on the asphalt layer rutting prediction are shown in figure 18 for the city of Woodbine, Georgia. For case 1 (unmodified PMED), the AR estimate was 0.07 inch. When the shortwave radiation model was updated (case 2), the AR estimate increased to 0.11 inch. After the D-LWR model was modified (case 3), the AR estimate increased to 0.20 inch. As a result of changing the U-LWR model (case 4), the AR estimate decreased to 0.03 inch. When both the U-LWR and D-LWR models were updated with constant-value vapor pressure data (case 5), the AR estimate increased to 0.15 inch. After the D-LWR model was updated with dynamic vapor pressure data (case 6), the AR estimate increased to 0.23 inch. Finally, as a result of

using the U-LWR and D-LWR models with dynamic vapor pressure data (case 7), the AR estimate was 0.16 inch.

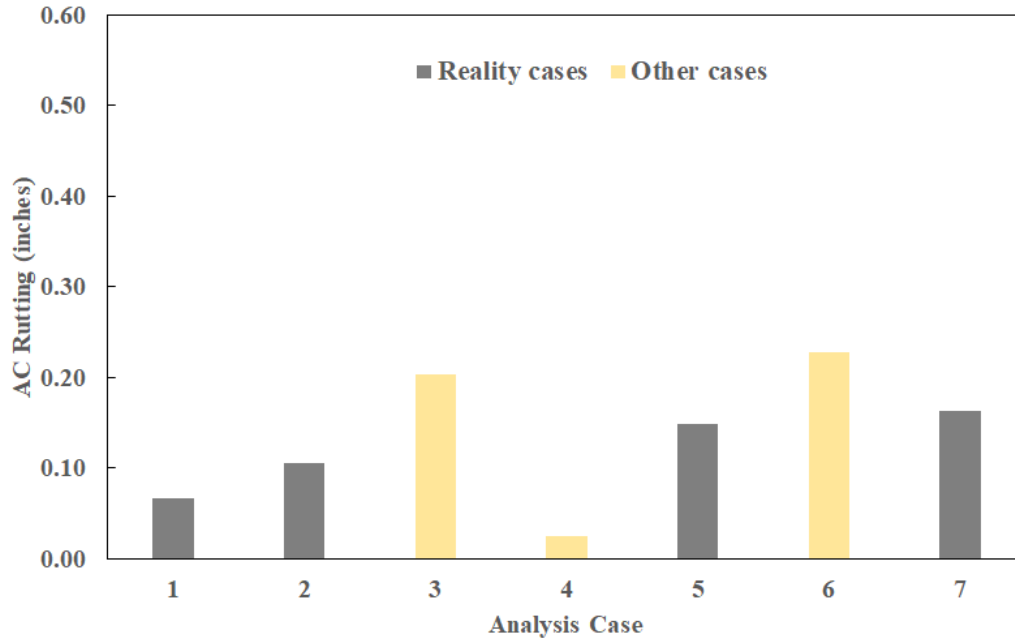


Figure 18. Graph. Impacts of radiation models on asphalt layer rutting prediction in Woodbine, GA.

Bottom-up Fatigue Cracking Predictions

The impacts of the shortwave and longwave radiation models on the bottom-up fatigue cracking prediction are shown in figure 19 for the city of Clayton, Georgia. For case 1 (unmodified PMED), the BUFC estimate was 0.02 percent. When the shortwave radiation model was updated (case 2), the BUFC estimate increased to 0.07 percent. After the D-LWR model was modified (case 3), the BUFC estimate increased to 0.31 percent. As a result of changing the U-LWR model (case 4), the BUFC estimate decreased to 0.00 percent. When both the U-LWR and D-LWR models were updated with constant-value vapor pressure data (case 5), the BUFC estimate increased to 0.15 percent. After the

D-LWR model was updated with dynamic vapor pressure data (case 6), the BUFC estimate increased to 0.35 percent. Finally, as a result of using the U-LWR and D-LWR models with dynamic vapor pressure data (case 7), the BUFC estimate was 0.15 percent.

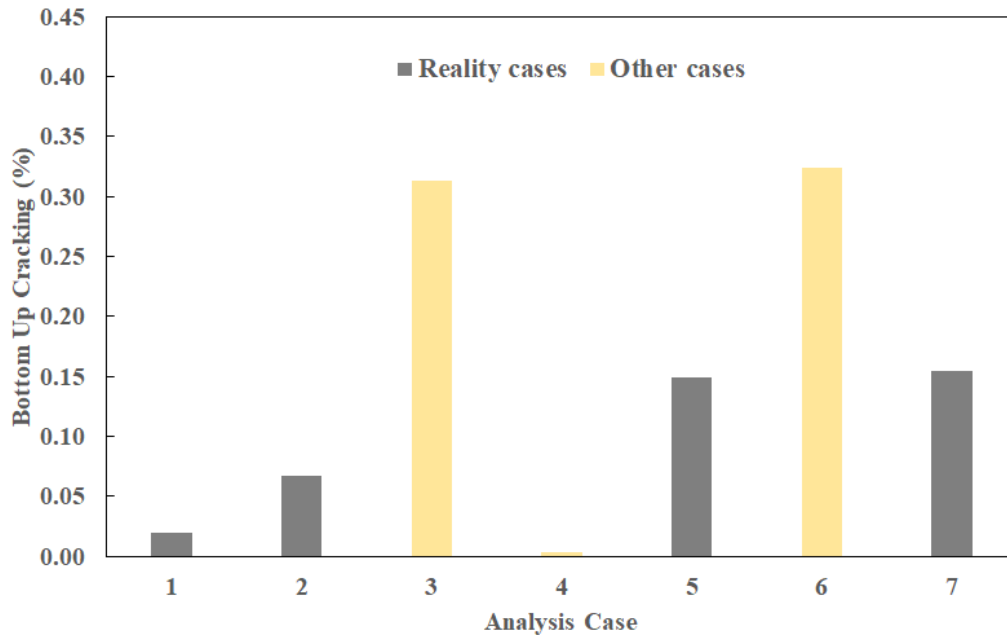


Figure 19. Graph. Impacts of radiation models on bottom-up fatigue cracking prediction in Clayton, GA.

The impacts of the shortwave and longwave radiation models on the bottom-up fatigue cracking prediction are shown in figure 20 for the city of Donalsonville, Georgia. For case 1 (unmodified PMED), the BUFC estimate was 0.02 percent. When the shortwave radiation model was updated (case 2), the BUFC estimate increased to 0.06 percent. After the D-LWR model was modified (case 3), the BUFC estimate increased to 0.29 percent. As a result of changing the U-LWR model (case 4), the BUFC estimate decreased to 0.00 percent. When both the U-LWR and D-LWR models were updated with constant-value vapor pressure data (case 5), the BUFC estimate increased to 0.14 percent. After the D-LWR model was updated with dynamic vapor pressure data (case 6), the BUFC estimate

increased to 0.33 percent. Finally, as a result of using the U-LWR and D-LWR models with dynamic vapor pressure data (case 7), the BUFC estimate was 0.17 percent.

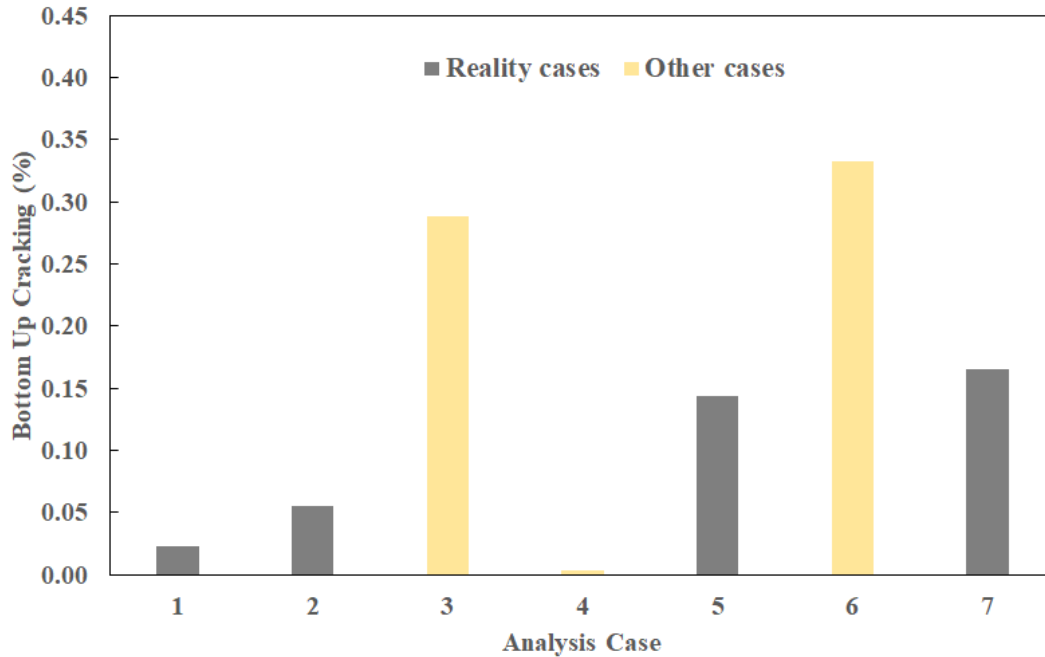


Figure 20. Graph. Impacts of radiation models on bottom-up fatigue cracking prediction in Donalsonville, GA.

The impacts of the shortwave and longwave radiation models on the bottom-up fatigue cracking prediction are shown in figure 21 for the city of Jeffersonville, Georgia. For case 1 (unmodified PMED), the BUFC estimate was 0.02 percent. When the shortwave radiation model was updated (case 2), the BUFC estimate increased to 0.05 percent. After the D-LWR model was modified (case 3), the BUFC estimate increased to 0.22 percent. As a result of changing the U-LWR model (case 4), the BUFC estimate decreased to 0.00 percent. When both the U-LWR and D-LWR models were updated with constant-value vapor pressure data (case 5), the BUFC estimate increased to 0.12 percent. After the D-WR model was updated with dynamic vapor pressure data (case 6), the BUFC estimate

increased to 0.25 percent. Finally, as a result of using the U-LWR and D-LWR models with dynamic vapor pressure data (case 7), the BUFC estimate was 0.13 percent.

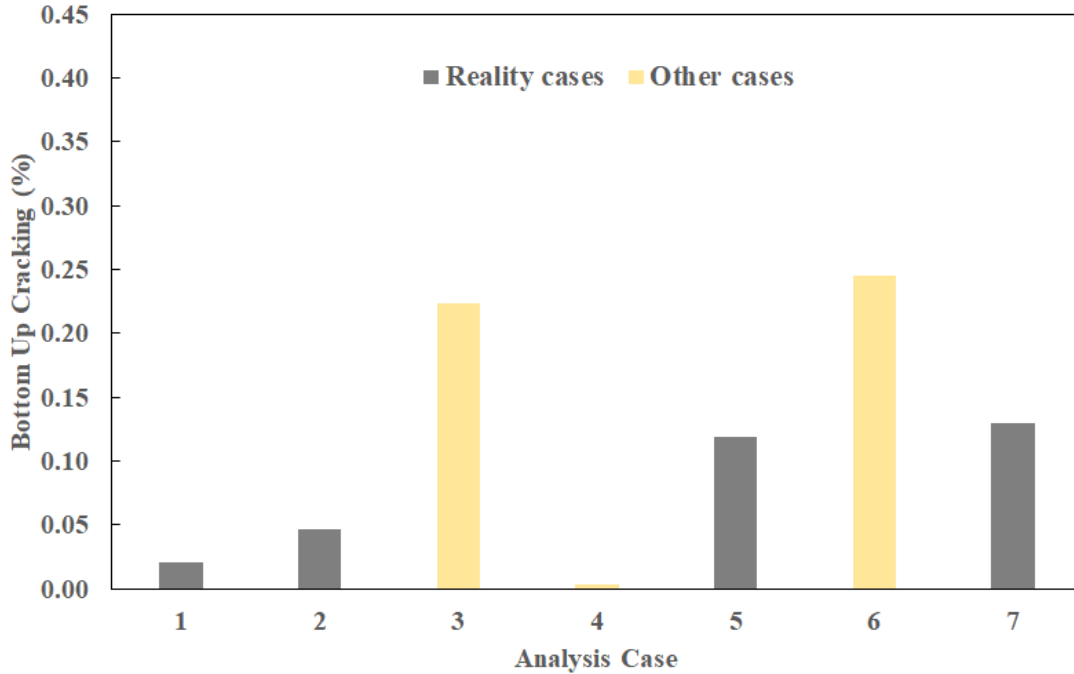


Figure 21. Graph. Impacts of radiation models on bottom-up fatigue cracking prediction in Jeffersonville, GA.

The impacts of the shortwave and longwave radiation models on the bottom-up fatigue cracking prediction are shown in figure 22 for the city of Trenton, Georgia. For case 1 (unmodified PMED), the BUFC estimate was 0.02 percent. When the shortwave radiation model was updated (case 2), the BUFC estimate increased to 0.07 percent. After the D-LWR model was modified (case 3), the BUFC estimate increased to 0.37 percent. As a result of changing the U-LWR model (case 4), the BUFC estimate decreased to 0.00 percent. When both the U-LWR and D-LWR models were updated with constant-value vapor pressure data (case 5), the BUFC estimate increased to 0.17 percent. After the D-LWR model was updated with dynamic vapor pressure data (case 6), the BUFC estimate

increased to 0.39 percent. Finally, as a result of using the U-LWR and D-LWR models with dynamic vapor pressure data (case 7), the BUFC estimate was 0.19 percent.

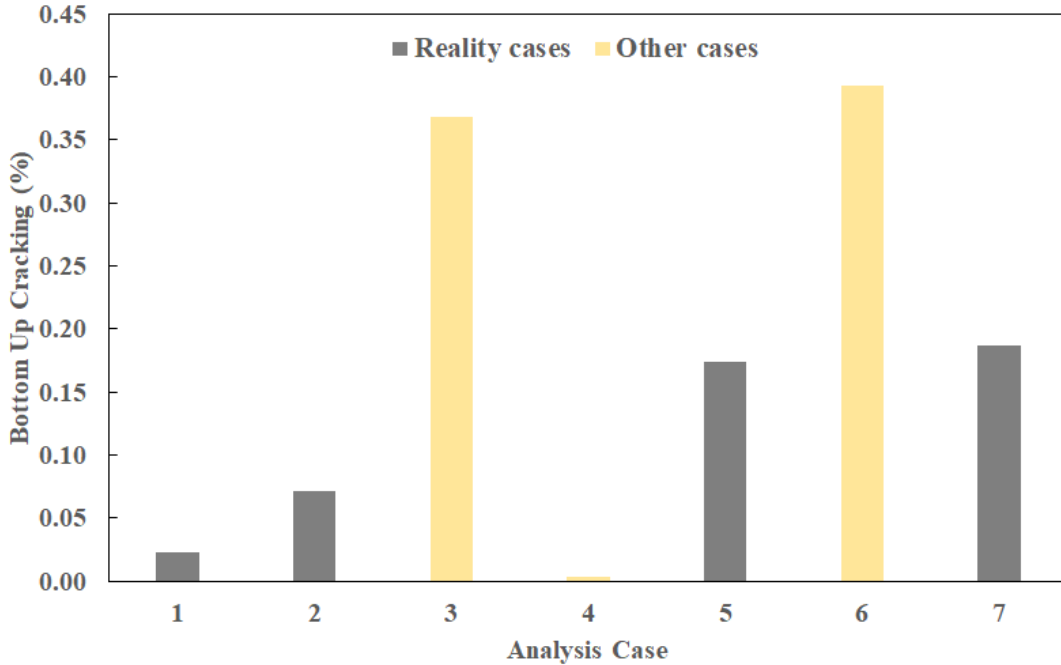


Figure 22. Graph. Impacts of radiation models on bottom-up fatigue cracking prediction in Trenton, GA.

The impacts of the shortwave and longwave radiation models on the bottom-up fatigue cracking prediction are shown in figure 23 for the city of Woodbine, Georgia. For case 1 (unmodified PMED), the BUFC estimate was 0.02 percent. When the shortwave radiation model was updated (case 2), the BUFC estimate increased to 0.04 percent. After the D-LWR model was modified (case 3), the BUFC estimate increased to 0.19 percent. As a result of changing the U-LWR model (case 4), the BUFC estimate decreased to 0.00 percent. When both the U-LWR and D-LWR models were updated with constant-value vapor pressure data (case 5), the BUFC estimate increased to 0.10 percent. After the D-LWR model was updated with dynamic vapor pressure data (case 6), the BUFC estimate

increased to 0.22 percent. Finally, as a result of using the U-LWR and D-LWR models with dynamic vapor pressure data (case 7), the BUFC estimate was 0.11 percent.

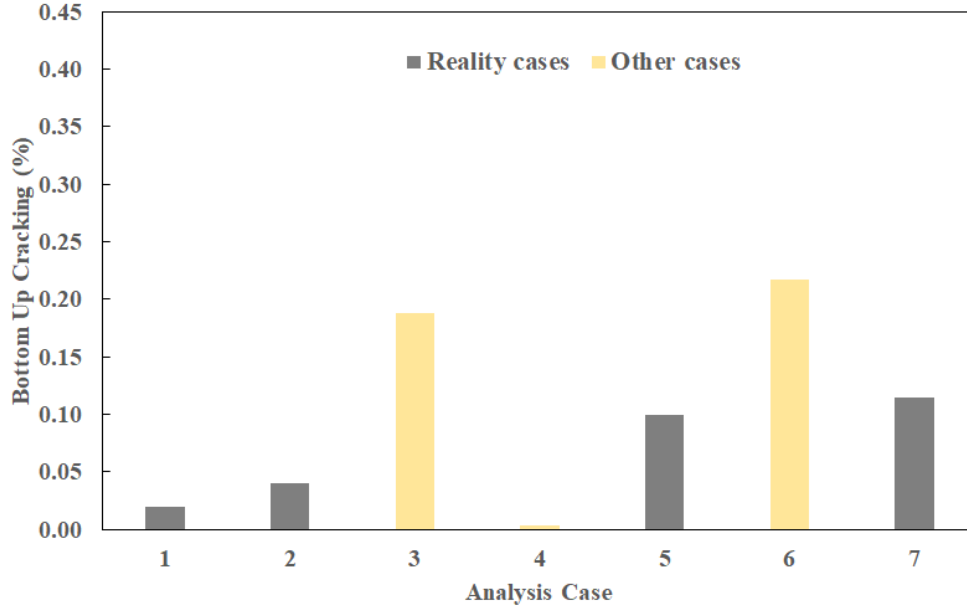


Figure 23. Graph. Impacts of radiation models on bottom-up fatigue cracking prediction in Woodbine, GA.

Pavement Surface Temperature Predictions

The impacts of the shortwave and longwave radiation models on the pavement surface temperature prediction are shown in figure 24 for the city of Clayton, Georgia. For case 1 (unmodified PMED), the average pavement surface temperature was 18.5°C. When the shortwave radiation model was updated (case 2), the average pavement surface temperature increased to 23.6°C. After the D-LWR model was modified (case 3), the average pavement surface temperature increased to 33.5°C. As a result of changing the U-LWR model (case 4), the average pavement surface temperature decreased to 3.3°C. When both the U-LWR and D-LWR models were updated with constant-value vapor pressure data (case 5), the average pavement surface temperature increased to 29.4°C.

After the D-LWR model was updated with dynamic vapor pressure data (case 6), the average pavement surface temperature increased to 33.0°C. Finally, as a result of using the U-LWR and D-LWR models with dynamic vapor pressure data (case 7), the average pavement surface temperature was 28.8°C.

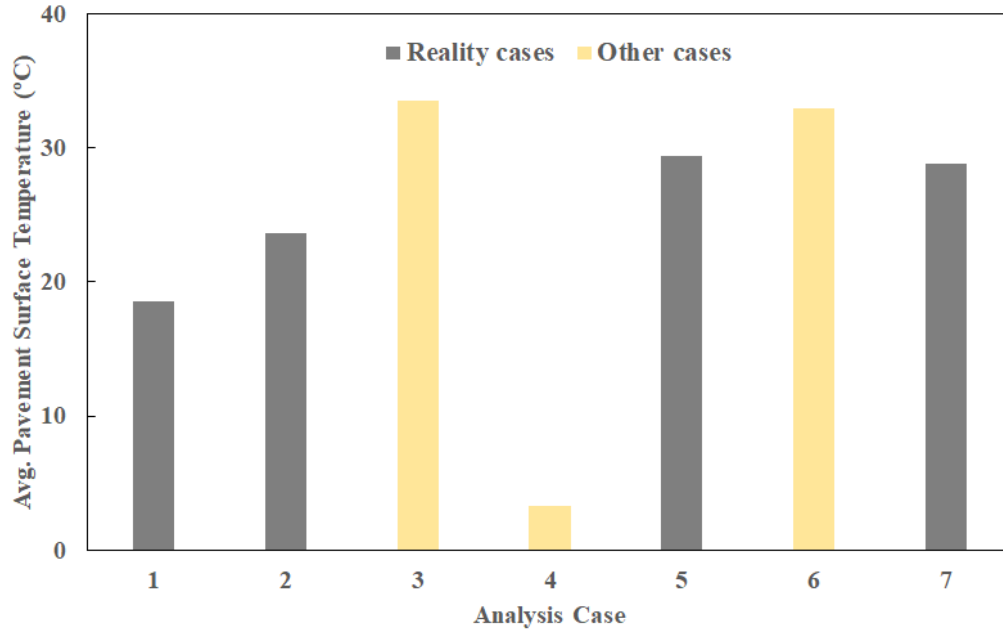


Figure 24. Graph. Impacts of radiation models on pavement surface temperature in Clayton, GA.

The impacts of the shortwave and longwave radiation models on the pavement surface temperature prediction are shown in figure 25 for the city of Donalsonville, Georgia. For case 1 (unmodified PMED), the average pavement surface temperature was 21.4°C. When the shortwave radiation model was updated (case 2), the average pavement surface temperature increased to 25.2°C. After the D-LWR model was modified (case 3), the average pavement surface temperature increased to 35.0°C. As a result of changing the U-LWR model (case 4), the average pavement surface temperature decreased to 7.3°C. When both the U-LWR and D-LWR models were updated with constant-value vapor

pressure data (case 5), the average pavement surface temperature increased to 31.3°C. After the D-LWR model was updated with dynamic vapor pressure data (case 6), the average pavement surface temperature increased to 35.2°C. Finally, as a result of using the U-LWR and D-LWR models with dynamic vapor pressure data (case 7), the average pavement surface temperature was 31.4°C.

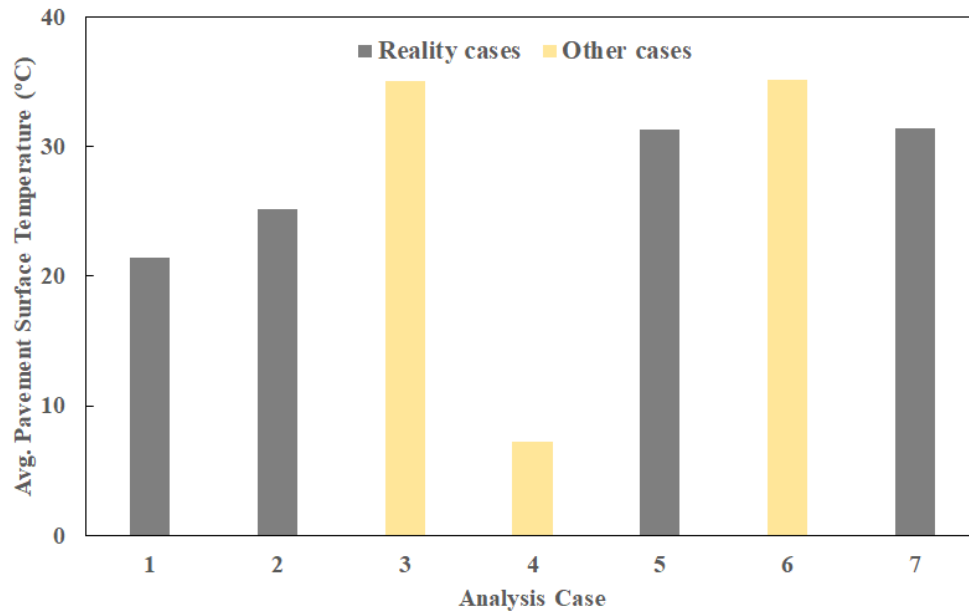


Figure 25. Graph. Impacts of Radiation Models on Pavement Surface Temperature in Donalsonville, GA

The impacts of the shortwave and longwave radiation models on the pavement surface temperature are shown in figure 26 for the city of Jeffersonville, Georgia. For case 1 (unmodified PMED), the average pavement surface temperature was 20.2°C. When the shortwave radiation model was updated (case 2), the average pavement surface temperature increased to 25.3°C. After the D-LWR model was modified (case 3), the average pavement surface temperature increased to 32.8°C. As a result of changing the U-LWR model (case 4), the average pavement surface temperature decreased to 7.4°C.

When both the U-LWR and D-LWR models were updated with constant-value vapor pressure data (case 5), the average pavement surface temperature increased to 29.4°C. After the D-LWR model was updated with dynamic vapor pressure data (case 6), the average pavement surface temperature increased to 32.7°C. Finally, as a result of using the U-LWR and D-LWR models with dynamic vapor pressure data (case 7), the average pavement surface temperature was 29.3°C.

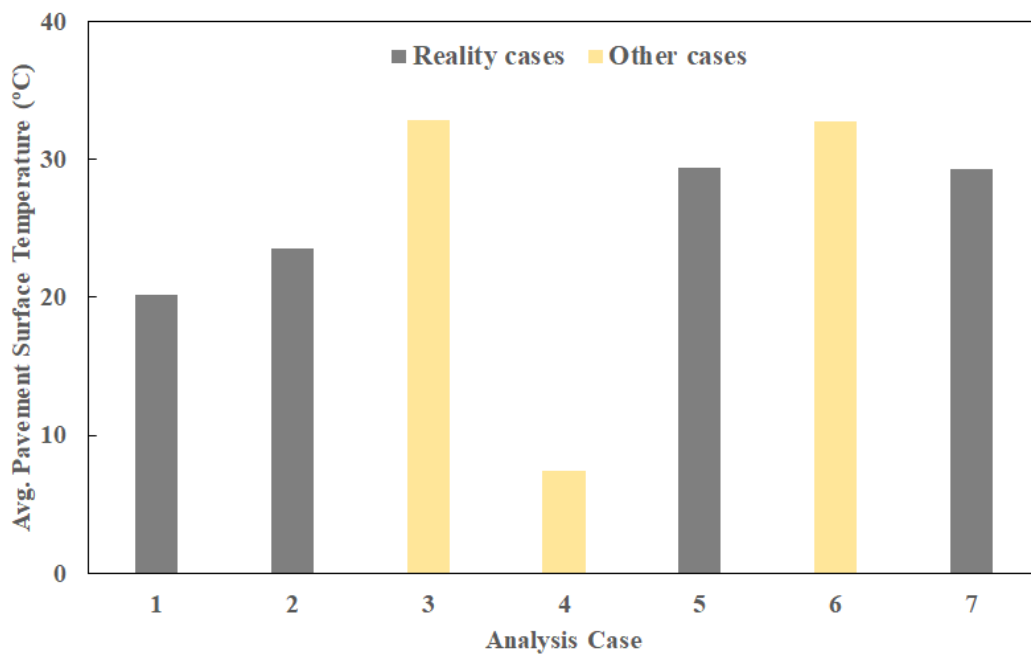


Figure 26. Graph. Impacts of radiation models on pavement surface temperature prediction in Jeffersonville, GA.

The impacts of the shortwave and longwave radiation models on the pavement surface temperature prediction are shown in figure 27 for the city of Trenton, Georgia. For case 1 (unmodified PMED), the average pavement surface temperature was 19.1°C. When the shortwave radiation model was updated (case 2), the average pavement surface temperature increased to 24.1°C. After the D-LWR model was modified (case 3), the

average pavement surface temperature increased to 34.4°C. As a result of changing the U-LWR model (case 4), the average pavement surface temperature decreased to 3.1°C. When both the U-LWR and D-LWR models were updated with constant-value vapor pressure data (case 5), the average pavement surface temperature increased to 30.2°C. After the D-LWR model was updated with dynamic vapor pressure data (case 6), the average pavement surface temperature increased to 34.0°C. Finally, as a result of using the U-LWR and D-LWR models with dynamic vapor pressure data (case 7), the average pavement surface temperature was 29.8°C.

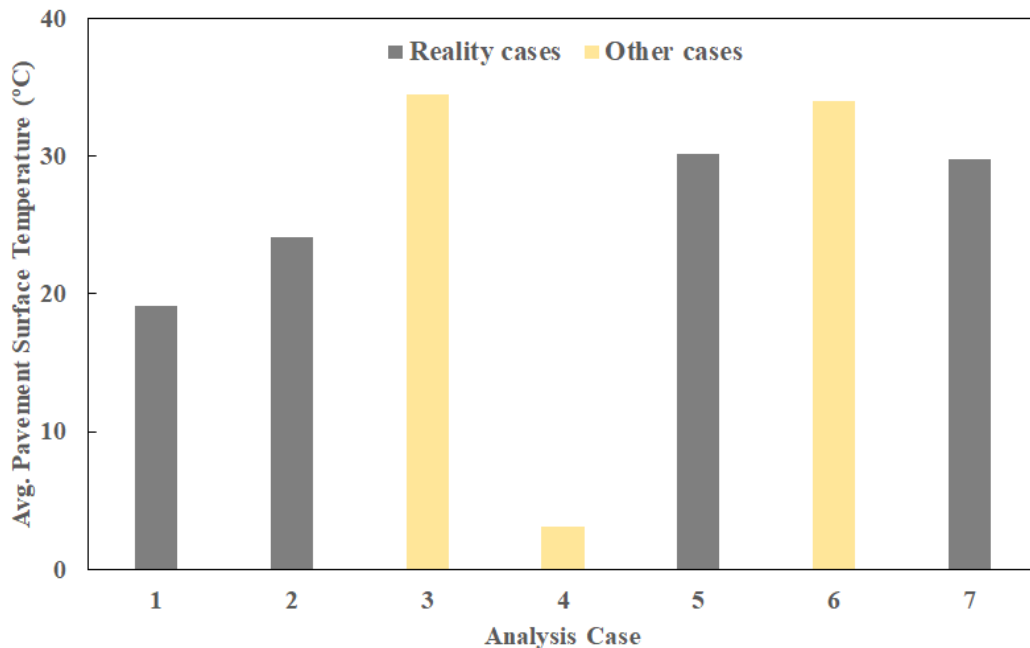


Figure 27. Graph. Impacts of radiation models on pavement surface temperature prediction in Trenton, GA.

The impacts of the shortwave and longwave radiation models on the pavement surface temperature prediction are shown in figure 28 for the city of Woodbine, Georgia. For case 1 (unmodified PMED), the average pavement surface temperature was 21.5°C.

When the shortwave radiation model was updated (case 2), the average pavement surface temperature increased to 24.4°C. After the D-LWR model was modified (case 3), the average pavement surface temperature increased to 33.4°C. As a result of changing the U-LWR model (case 4), the average pavement surface temperature decreased to 9.1°C. When both the U-LWR and D-LWR models were updated with constant-value vapor pressure data (case 5), the average pavement surface temperature increased to 30.1°C. After the D-LWR model was updated with dynamic vapor pressure data (case 6), the average pavement surface temperature increased to 33.7°C. Finally, as a result of using the U-LWR and D-LWR models with dynamic vapor pressure data (case 7), the average pavement surface temperature was 30.4°C.

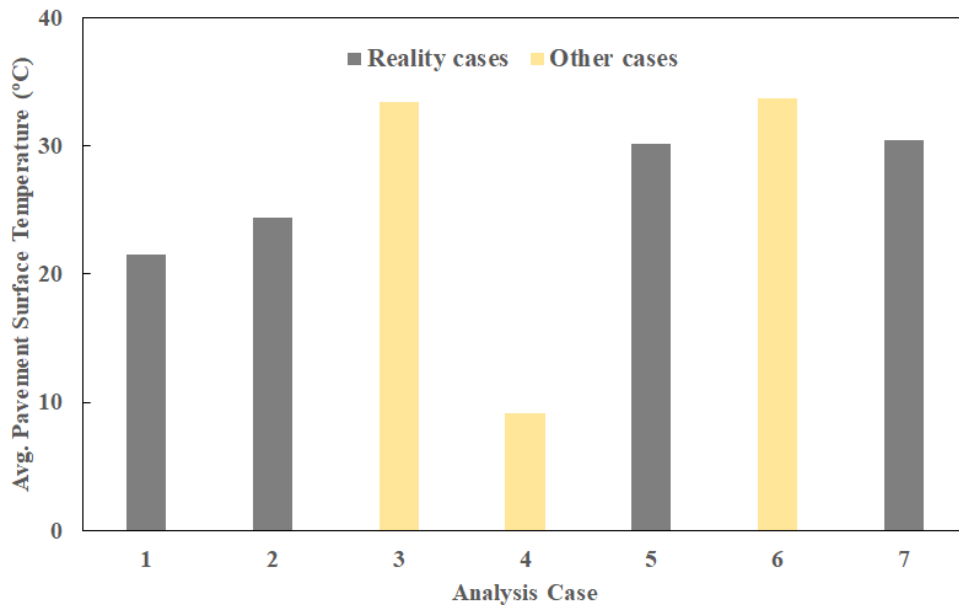


Figure 28. Graph. Impacts of radiation models on pavement surface temperature prediction in Woodbine, GA.

CHAPTER 5. CONCLUSIONS AND RECOMMENDATIONS

SUMMARY AND CONCLUSIONS

In PMED, the net SWR, D-LWR, and U-LWR are estimated based on empirical relationships. In this study, the accuracy of the empirical radiation models was assessed and compared, along with alternative radiation models. Ground-based radiation observations were collected from the SIRS stations for comparisons. The accuracies of the D-SWR and D-LWR models were determined using RMSE and bias values. In addition, the sensitivity of different radiation models on asphalt pavement distress predictions were investigated. A mechanistic–empirical pavement analysis software called MEAPA was utilized for computations. Seven analyses cases were defined based on different radiation models. Case 1 reflects the unmodified PMED D-SWR model. Case 2 corresponds to the modified D-SWR model. Cases 3 and 4 represent the modified D-LWR and U-LWR models, respectively. Case 5 reflects the modified D-SWR, D-LWR, and U-LWR model. Case 6 corresponds to the modified D-LWR model with dynamic vapor pressure data. Case 7 is identical to case 5 other than that in case 5 the D-LWR was calculated assuming a constant vapor pressure value of 10 mm Hg, whereas case 7 utilizes hourly vapor pressure data from MERRA-2 to calculate the D-LWR.

In this chapter, pavement distress predictions for analysis cases 1, 2, 5, and 7 are highlighted since the remainder of the cases represent hypothetical conditions. Detailed pavement distress predictions for all cases (including cases 3, 4, and 6) are provided in chapter 4. The findings from this study are summarized as follows:

1. MERRA-2 SWR estimates were in satisfactory agreement with ground-based SIRS observations. SWR estimates from PMED were noticeably different from MERRA-2 products.
2. Idso (1981) D-LWR estimates showed excellent agreement with SIRS measurements. The PMED-recommended D-LWR (Dempsey et al. 1985) estimates did not agree well with the SIRS measurements. The Dempsey et al. (1985) D-LWR model is physically inconsistent since the cloud cover effects appear to be in the wrong direction. If the air temperature is assumed constant, the presence of clouds increases the amount of precipitable water that, subsequently, increases the emissivity of the atmosphere. As a result, the amount of D-LWR that reaches the pavement surface is increased. However, the Dempsey et al. (1985) model systematically attenuates the D-LWR estimates because of incorrect cloud base factor.
3. The PMED-recommended U-LWR model includes a cloud base factor, which is an incorrect assumption. In reality, U-LWR emission is a function of the pavement surface temperature, which is not influenced by the presence of clouds. In this study, the U-LWR model was modified based on a more physically consistent parameterization that did not include any cloud base factor.
4. Based on these results, it was determined that PMED radiation models (case 1) were physically inconsistent. In this report, the pavement distresses for all analysis cases were predicted using the PMED global calibration coefficients. It was evidenced that the pavement distresses were considerably

influenced as a result of updating the radiation models. For instance, the total rutting, asphalt layer rutting, and bottom-up fatigue cracking distresses were increased by 1.3, 2, and 2.7 times, respectively, after updating the D-SWR model (case 2). As a result of using a modified D-LWR model assuming constant vapor pressure data (case 5), the total rutting, asphalt layer rutting, and bottom-up fatigue cracking distresses were further increased by 1.2, 1.4, and 2.4 times, respectively. The total rutting, asphalt layer rutting, and bottom-up fatigue cracking distress predictions were additionally increased by 1.05, 1.09, and 1.10 times, respectively, by using a modified D-LWR model with time-varying vapor pressure (case 7). The results suggested that the total rutting, asphalt layer rutting, and bottom-up fatigue cracking estimates were more influenced by using the updated D-SWR model (case 2) compared to updated D-LWR models (cases 5 and 7). However, these results do not indicate that the in-field pavement distresses will be increased as a result of utilizing the modified radiation models. After the PMED global coefficients are recalibrated for modified radiation models, the pavement distress predictions will represent the in-field condition.

5. The pavement temperatures were considerably increased with the updated D-SWR model (case 2) since the D-SWR (sunlight) impacts the pavement temperature during the daytime. The asphalt rutting was highly sensitive to the modified D-SWR model. Sensitivity of total rutting and bottom-up fatigue cracking were moderate to high and insignificant, respectively.

6. The pavement temperatures were noticeably increased as a result of using the modified D-LWR models (cases 5 and 7) since D-LWR impacts the pavement temperature during the nighttime. The asphalt and total rutting estimates showed mild sensitivity to updated D-LWR and U-LWR models, and the sensitivity of the bottom-up fatigue cracking was negligible.
7. The subdiurnal vapor pressure varies significantly in subtropical humid regions such as Georgia. As a result, the asphalt pavement distresses were mildly sensitive to the D-LWR model with a time-variable vapor pressure (case 7) compared to the D-LWR model assuming constant-value vapor pressure data (case 5).

RECOMMENDATIONS

Based on the results, this study recommends the replacement of the D-SWR, D-LWR, and U-LWR models that are currently followed in PMED with the radiation models that were utilized in analysis case 7. The PMED radiation models are sometimes physically inconsistent and inaccurate, as evidenced in this study. The pavement temperature profiles computed using these radiation models, and as a consequence, the predicted pavement distresses, are substantially different from those computed using the less accurate and physically inconsistent PMED models. To facilitate these recommendations, a step by step comprehensive guideline is provided for extraction of MERRA-2 data from the U.S. National Aeronautics and Space Administration (NASA) servers in APPENDIX A: Extraction of MERRA-2 and for implementation and integration of modified SWR and LWR models in PMED in APPENDIX B: Implementation and Integration of SWR and LWR Models in PMED.

APPENDICES

APPENDIX A: EXTRACTION OF MERRA-2 DATA

INTRODUCTION

The Modern Era Retrospective Analysis for Research and Applications (MERRA) is a state-of-the-art atmospheric data reanalysis product. The MERRA dataset is developed by the U.S. National Aeronautics and Space Administration (NASA). The MERRA product provides climatic data at 1-hour intervals since 1979. Since 2016, the advanced MERRA, version 2 (MERRA-2) dataset is available. The MERRA-1 and MERRA-2 data provide all the necessary climate input required by the Pavement ME Design (PMED) software. This manual provides step-by-step guidance to extract the MERRA-2 climate data in a PMED-compatible format.

BACKGROUND

Extraction of MERRA-2 data from NASA servers requires the users to write their own programming codes using languages such as Python, MATLAB, IDL, etc. In addition, some MERRA-2 data units need to be converted to conventional weather units common to infrastructure uses. For instance, precipitation in MERRA-2 is expressed as mass/(area*time), whereas rain is traditionally measured by inches per hour or day. The Federal Highway Administration (FHWA) has developed a tool called the long-term pavement performance (LTPP) climate data tool (Schwartz 2015), which can extract MERRA-2 data in a PMED-compatible format. In addition, this tool does not require the users to write their own programming codes. This guideline provides guidance on MERRA-2 data extraction using the LTPP climate data tool.

EXTRACT AND DOWNLOAD MERRA-2 DATA

- **Step 1:** Visit the webpage (<https://infopave.fhwa.dot.gov/Data/ClimateTool>).
- **Step 2:** Select the location of interest as shown in figure 29. Type the name of the place (red arrow) or utilize single-point data selection (black arrow) or area data selection (yellow arrow). Zoom in and out of the map as needed (green arrow).
- **Step 3:** Scroll down after a location is selected. Select the date range, check ‘Show Advanced Data Classification’, check all data attributes of interest, and click ‘Add to Selection’ (figure 30).
- **Step 4:** Scroll down and click ‘Add to Data Bucket’ (figure 31).
- **Step 5:** Scroll down and click ‘Go to Data Bucket’ (figure 32).
- **Step 6:** Scroll down, provide an email address and preferred file format (such as Microsoft Excel, Access, or SQL) and unit system. Complete the security check and click ‘Submit for Data Extraction’ (figure 33). User will be notified via email when the data are ready for download.

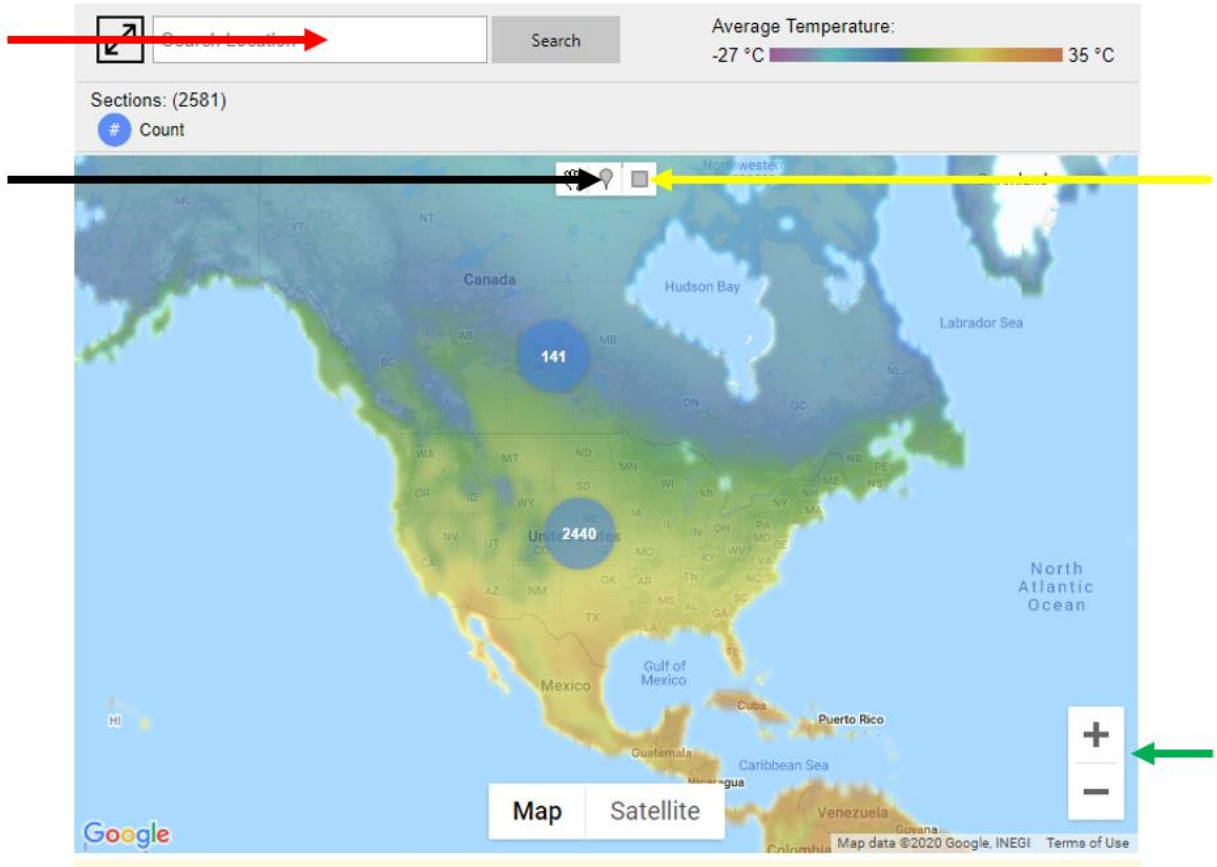


Figure 29. Image. LTPP climate tool page.

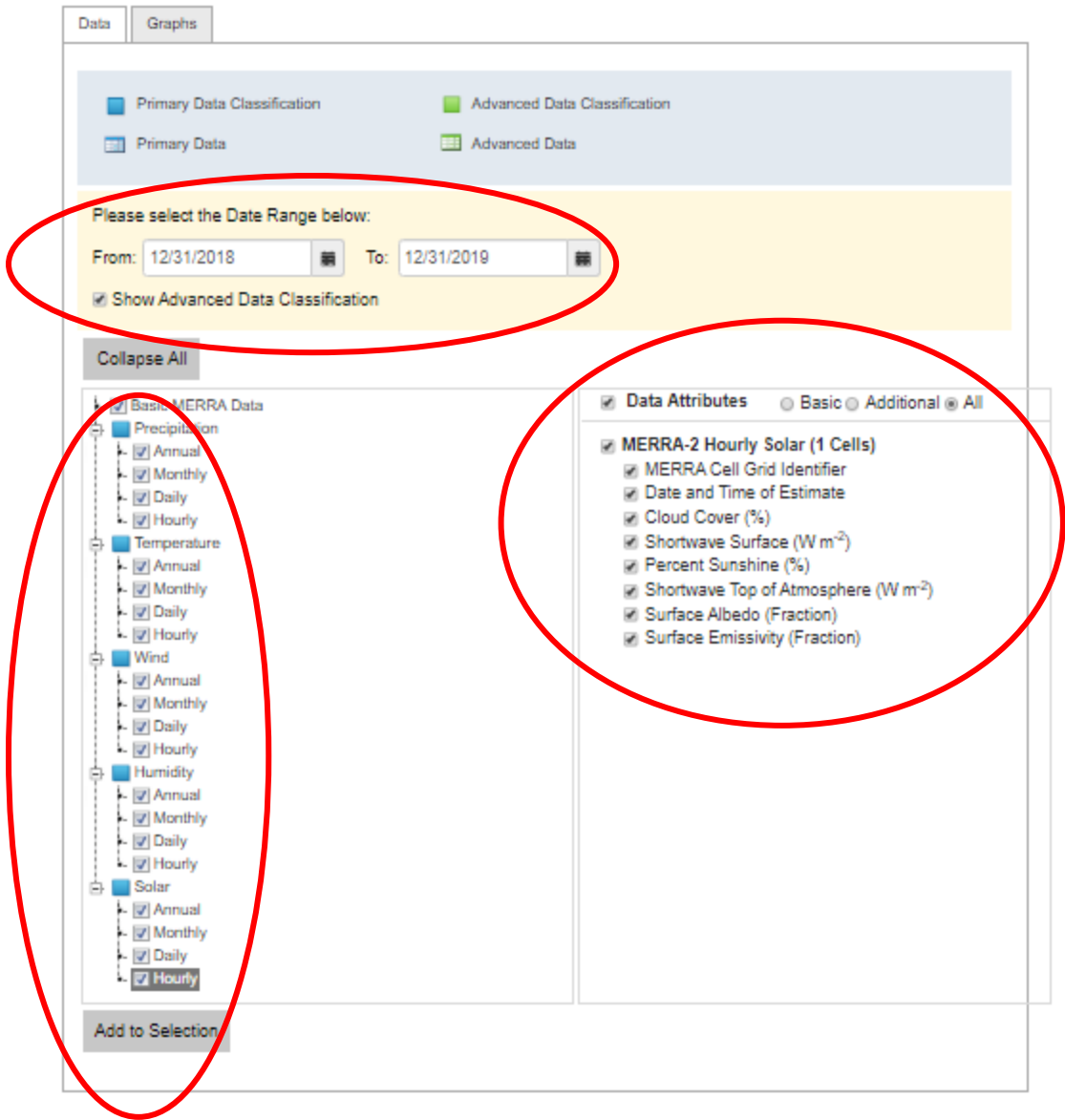


Figure 30. Image. Data attributes selection.

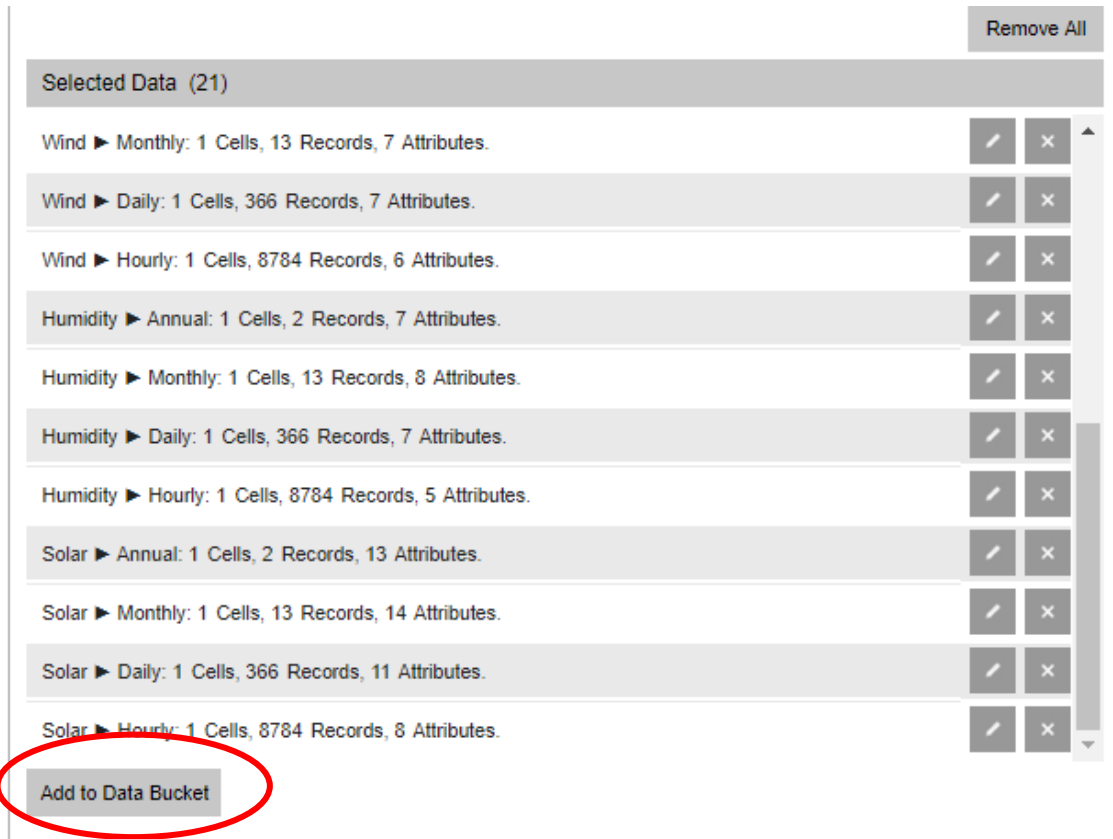


Figure 31. Image. Add to data bucket.

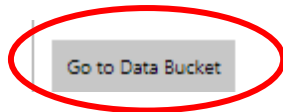


Figure 32. Image. Go to data bucket.

Data Export

If you provide your e-mail address, the system will notify you when your Data Bucket is ready for download. Otherwise, please remember to save the Bucket Number generated in the next page in order to track your Data Bucket later. You can check the status of your Data Bucket on the on [Data Bucket Tracker](#) page.

Email Address:

Export File Format:

Unit System: As-Collected Metric US Customary

Include values of coded data elements.

Comments:


Security Check: 

Figure 33. Image. Submit for data extraction.

The data acquisition instructions outlined here are current as of November 1, 2020. However, NASA routinely makes changes to how the scientific community accesses its publicly available data; hence, the methods outlined here are not guaranteed to work in perpetuity.

APPENDIX B: IMPLEMENTATION AND INTEGRATION OF SWR AND LWR MODELS IN PMED

SHORTWAVE RADIATION MODEL

Current practice:

The net shortwave radiation (SWR) is analyzed based on empirical relationships as shown in equation A.1 (Dempsey et al. 1985).

$$Q_s = a_s * R * (A + \frac{BS_c}{100}) \quad (A.1)$$

where, Q_s is net shortwave radiation; a_s is surface shortwave absorptivity of the pavement surface; R is extraterrestrial radiation incident at the top of the atmosphere; A, B are diffuse scattering and adsorption coefficients; and S_c is percent sunshine.

Recommended practice:

Obtain downwelling shortwave radiation (D-SWR) from MERRA-2 and calculate net SWR as shown in equation A.2 (Dempsey et al. 1985).

$$Q_s = a_s * Q_i \quad (A.2)$$

where, Q_s is net SWR, a_s is surface shortwave absorptivity of the pavement surface, ($a_s = 1 - Albedo$), and Q_i is the D-SWR that is a product of the MERRA-2 reanalysis.

Summary:

Replace equation A.1 in the Pavement ME Design background analysis with equation A.2.

DOWNWELLING LONGWAVE RADIATION MODEL

Current practice:

The downwelling longwave radiation (D-LWR) for the clear-sky condition is determined based on the relationships as shown in equation A.3 (Unsworth 1975).

$$Q_z = \sigma_{sb} * \epsilon * T_{air}^4 \quad (A.3)$$

where, Q_z is downwelling longwave radiation without cloud cover correction, σ_{sb} is the Stefan–Boltzmann constant, ϵ is atmospheric emissivity, and T_{air} is air temperature.

The atmospheric emissivity is determined based on empirical relationships, as shown in equation A.4 (Dempsey et al. 1985).

$$\epsilon_D = (G - \frac{J}{10\rho p}) \quad (A.4)$$

where, ϵ_D is atmospheric emissivity parameterization proposed by Dempsey et al. (1985); G , J , ρ are regression coefficients; and p is vapor pressure of air (1 to 10 mm Hg).

The D-LWR for the all-sky condition is determined as shown in equation A.5 (Dempsey et al. 1985).

$$Q_a = Q_z * (1 - \frac{N_D W}{100}) \quad (A.5)$$

where, Q_a is downwelling longwave radiation with cloud cover correction, Q_z is downwelling longwave radiation without cloud cover correction, N_D (= 0.8 to 0.9) is the cloud base factor proposed by Dempsey et al. (1985), and W is cloud cover.

Recommended practice:

Determine atmospheric emissivity based on a more physically consistent parameterization as shown in equation A.6. (Idso 1981).

$$\epsilon_l = a_l + b_l * p \quad (A.6)$$

where, ϵ_l is atmospheric emissivity parameterizations proposed by Idso (1981); a_l, b_l are regression coefficients proposed by Idso (1981); and p is vapor pressure of air (1 to 10 mm Hg).

Determine D-LWR under the all-sky condition based on the cloud amplification factor as shown in equation A.7 (Iziomon et al. 2003; Sugita and Brutsaert 1993).

$$Q_a = Q_z * \left(1 + \frac{NW}{100}\right) \quad (\text{A.7})$$

where, Q_a is downwelling longwave radiation with cloud cover correction, Q_z is downwelling longwave radiation without cloud cover correction, N ($= 0.17$) is the cloud amplification factor, and W is cloud cover.

Summary:

Replace equations A.4 and A.5 in the PMED background analysis with equations A.6 and A.7, respectively. Leave equation A.3 as is.

UPWELLING LONGWAVE RADIATION MODEL

Current practice:

The upwelling longwave radiation (U-LWR) for the clear and all-sky conditions are calculated as shown in equations A.8 and A.9, respectively (Dempsey et al. 1985).

$$Q_x = \sigma_{sb} * \epsilon * T_s^4 \quad (\text{A.8})$$

$$Q_e = Q_x * \left(1 - \frac{N_D W}{100}\right) \quad (\text{A.9})$$

where, Q_x is upwelling longwave radiation without cloud cover correction, Q_e is upwelling longwave radiation with cloud cover correction, ϵ is emissivity of the pavement, T_s is surface temperature, N_D ($= 0.8$ to 0.9) is the cloud base factor proposed by Dempsey et al. (1985), W is cloud cover, and σ_{sb} is the Stefan–Boltzmann constant.

Recommended practice:

Utilize a more physically consistent parameterization for U-LWR under the all-sky condition, as shown in equation A.10, since cloud presence has no effect on U-LWR (Koll and Cronin 2018).

$$Q_e = Q_x = \sigma_{sb} * \epsilon * T_s^4 \quad (\text{A.10})$$

where, Q_x is upwelling longwave radiation without cloud cover correction, Q_e is upwelling longwave radiation with cloud cover correction, ϵ is emissivity of the pavement, T_s is surface temperature, and σ_{sb} is the Stefan–Boltzmann constant.

Summary:

Replace equation A.9 in the PMED background analysis with equation A.10. Leave equation A.8 as is.

ACKNOWLEDGMENTS

The University of Georgia, Michigan State University, and the University of Maryland acknowledge the financial support for this work provided by the Georgia Department of Transportation. The authors also thank the many GDOT personnel who assisted with this study. A special thanks is offered to GDOT personnel Ian Rish, State Pavement Engineer; Sunil Thapa, Research Specialist; and Supriya Kamatkar, Assistant Office Head. In addition, the authors thank M. Emin Kutay, Professor at Michigan State University, for assistance in this project.

REFERENCES

- AASHTO. (1993). *Guide for Design of Pavement Structures*. American Association of State Highway and Transportation Officials, Washington, DC.
- . (2015). *Mechanistic–Empirical Pavement Design Guide—A Manual of Practice*. American Association of State Highway and Transportation Officials, Washington, DC.
- Anderson, D.B. (1936). "Relative Humidity or Vapor Pressure Deficit." *Ecology*, 17, pp. 277–282, Ecological Society of America, Washington, DC.
- Andrey, J., Hambly, D., Mills, B., and Afrin, S. (2013). "Insights into Driver Adaptation to Inclement Weather in Canada." *Journal of Transport Geography*, 28, pp. 192–203.
- Ångström, A.K. (1915). "A Study of the Radiation of the Atmosphere: Based upon Observations of the Nocturnal Radiation During Expeditions to Algeria and to California." *Smithsonian Miscellaneous Collections*, 65(3), pp. 1–159, Smithsonian Institution, Washington, DC.
- Breakah, T.M., Williams, R.C., Herzmann, D.E., and Takle, E.S. (2011). "Effects of Using Accurate Climatic Conditions for Mechanistic–Empirical Pavement Design." *Journal of Transportation Engineering*, 137(1), pp. 84–90.
- Brink, W., Von Quintus, H., and Osborne, Jr., L.F. (2017). "Updates to Hourly Climate Data for Use in AASHTOWare Pavement Mechanistic–Empirical Design." *Transportation Research Record: Journal of the Transportation Research Board*, 2640(1), pp. 11–20.
- Brunt, D. (1932). "Notes on Radiation in the Atmosphere. I." *Quarterly Journal of the Royal Meteorological Society*, 58(247), pp. 389–420.
- Cetin, B., Forman, B.A., Schwartz, C.W., and Ruppelt, B. (2018). "Performance of Different Climate Data Sources in Mechanistic–Empirical Pavement Distress Analyses." *Journal of Transportation Engineering, Part B: Pavements*, 144(1), 04017023.
- Dempsey, B.J., Herlache, W.A., and Patel, A.J. (1985). *Environmental Effects on Pavements: Theory Manual*. FHWA/RD-84-115, U.S. Department of Transportation, Federal Highway Administration, Washington, DC.
- Durham, S.A., Cetin, B., Schwartz, C.W., Forman, B., and Gopiseti, L.S.P. (2019). *Improvement of Climate Data for Use in MEPDG Calibration and Other Pavement Analysis*. FHWA-GA-19-1610, Georgia Department of Transportation, Atlanta, GA.
- Faisal, H.M., Khan, Z.H., and Tarefder, R. (2016). "Modeling Nanoscale Rheological and Mechanical Properties of Thin Film Asphalt Binder." *Proceedings of the ASME 2016 International Mechanical Engineering Congress and Exposition*, November 11–17, Phoenix, AZ, American Society of Mechanical Engineers, V010T013A013.

- Forman, B.A. and Margulis, S.A. (2009). "High-resolution Satellite-based Cloud-coupled Estimates of Total Downwelling Surface Radiation for Hydrologic Modelling Applications." *Hydrology & Earth System Sciences*, 13(7), pp. 969–986.
- . (2010). "Assimilation of Multiresolution Radiation Products into a Downwelling Surface Radiation Model: 1. Prior Ensemble Implementation." *Journal of Geophysical Research: Atmospheres*, 115(D22).
- Gelaro, R., McCarty, W., Suárez, M.J., Todling, R., et al. (2017). "The Modern-era Retrospective Analysis for Research and Applications, Version 2 (MERRA-2)." *Journal of Climate*, 30(14), pp. 5419–5454.
- Idso, S.B. (1981). "A Set of Equations for Full Spectrum and 8- to 14- μm and 10.5- to 12.5- μm Thermal Radiation from Cloudless Skies." *Water Resources Research*, 17(2), pp. 295–304.
- Islam, M.R., Mannan, U.A., Rahman, A., and Tarefder, R.A. (2014). "Simplified Thermal Stress Model to Predict Low Temperature Cracks in Flexible Pavement." *Pavement Materials, Structures, and Performance*, 239, Geotechnical Special Publication, pp. 251–261.
- Iziomon, M.G., Mayer, H., and Matzarakis, A. (2003). "Downward Atmospheric Longwave Irradiance Under Clear and Cloudy Skies: Measurement and Parameterization." *Journal of Atmospheric and Solar-Terrestrial Physics*, 65(10), pp. 1107–1116.
- Johanneck, L. and Khazanovich, L. (2010). "Comprehensive Evaluation of Effect of Climate in *Mechanistic–Empirical Pavement Design Guide* Predictions." *Transportation Research Record*, 2170, pp. 45–55.
- Kalnay, E., Kanamitsu, M., Kistler, R., et al. (1996). "The NCEP/NCAR 40-year Reanalysis Project." *Bulletin of the American Meteorological Society*, 77(3), pp. 437–472.
- Khan, Z., Faisal, H.M., and Tarefder, R. (2017a). "Fracture Toughness Measurement of Asphalt Concrete by Nanoindentation." *Proceedings of the 2017 International Mechanical Congress & Exposition*, Nov 3–9, Tampa, FL, American Society of Mechanical Engineers, V010T013A010.
- Khan, Z.H., Ahmed, M.U., and Tarefder, R.A. (2017b). "Properties of Asphalt Pavement Layers Through Field Instrumentation at I-40." *Transportation Research Board 96th Annual Meeting Compendium of Papers*, Washington, DC.
- Khan, Z.H., Islam, M.R., and Tarefder, R.A. (2019). "Determining Asphalt Surface Temperature Using Weather Parameters." *Journal of Traffic and Transportation Engineering (English Edition)*, 6(6), pp. 577–588.
- Koll, D.D.B. and Cronin, T.W. (2018). "Earth's Outgoing Longwave Radiation Linear Due to H₂O Greenhouse Effect." *Proceedings of the National Academy of Sciences*, 115(41), pp. 10293–10298.
- NASA. (2014). The NASA Earth's Energy Budget Poster. http://science-edu.larc.nasa.gov/energy_budget/. Accessed August 16, 2018.

- NCHRP. (2004). *Guide for Mechanistic–Empirical Design of New and Rehabilitated Pavement Structures*. Transportation Research Board, Washington, DC.
- Onogi, K., Koide, H., Sakamoto, M., et al. (2005). "JRA-25: Japanese 25-year Re-analysis Project—Progress and Status." *Quarterly Journal of the Royal Meteorological Society*, 131(613), pp. 3259–3268.
- Rienecker, M.M., Suárez, M.J., Gelaro, R., Todling, R., et al. (2011). "MERRA: NASA's Modern-Era Retrospective Analysis for Research and Applications." *Journal of Climate*, 24(14), pp. 3624–3648.
- Schwartz, C.W. (2015). *Evaluation of LTPP Climatic Data for Use in Mechanistic–Empirical Pavement Design Guide Calibration and Other Pavement Analysis*. Technical Report No. FHWA-HRT-15-019, U.S. Department of Transportation, Federal Highway Administration, Turner-Fairbank Highway Research Center, McLean, VA.
- Schwartz, C.W., Forman, B.A., and Leininger, C.W. (2015). "Alternative Source of Climate Data for Mechanistic–Empirical Pavement Performance Prediction." *Transportation Research Record: Journal of the Transportation Research Board*, 2524, pp. 83–91.
- Sugita, M., and Brutsaert, W. (1993). "Cloud Effect in the Estimation of Instantaneous Downward Longwave Radiation." *Water Resources Research*, 29(3), pp. 599–605.
- Unsworth, M.H. (1975). "Long-wave Radiation at the Ground. II. Geometry of Interception by Slopes, Solids, and Obstructed Planes." *Quarterly Journal of the Royal Meteorological Society*, 101(427), pp. 25–34.
- Uppala, S.M., Kållberg, P.W., Simmons, A.J., et al. (2005). "The ERA-40 Re-analysis." *Quarterly Journal of the Royal Meteorological Society*, 131(612), pp. 2961–3012.
- Várnai, T., and Davies, R. (1999). "Effects of Cloud Heterogeneities on Shortwave Radiation: Comparison of Cloud-Top Variability and Internal Heterogeneity." *Journal of the Atmospheric Sciences*, 56(24), pp. 4206–4224.
- Zaghloul, S., Aayed, A., Halim, A.A.E., Vitillo, N., and Sauber, R. (2006). "Investigations of Environmental and Traffic Impacts on *Mechanistic–Empirical Pavement Design Guide* Predictions." *Transportation Research Record: Journal of the Transportation Research Board*, 1967(1), pp. 148–159.